

# Constraining the reionization history with QSO absorption spectra

S. Gallerani<sup>\*</sup>, T. Roy Choudhury<sup>†</sup>, and A. Ferrara<sup>‡</sup>

*SISSA/ISAS, via Beirut 2-4, 34014 Trieste, Italy.*

8 December 2018

## ABSTRACT

We use a semi-analytical approach to simulate absorption spectra of QSOs at high redshifts with the aim of constraining the cosmic reionization history. We consider two physically motivated and detailed reionization histories: (i) an Early Reionization Model (ERM) in which the intergalactic medium is reionized by PopIII stars at  $z \approx 14$ , and (ii) a more standard Late Reionization Model (LRM) in which overlapping, induced by QSOs and normal galaxies, occurs at  $z \approx 6$ . From the analysis of current Ly $\alpha$  forest data at  $z < 6$ , we conclude that it is impossible to disentangle the two scenarios, which fit equally well the observed Gunn-Peterson optical depth, flux probability distribution function and dark gap width distribution. At  $z > 6$ , however, clear differences start to emerge which are best quantified by the dark gap and peak width distributions. We find that 35 (zero) per cent of the lines of sight within  $5.7 < z < 6.3$  show dark gaps widths  $> 50\text{\AA}$  in the rest frame of the QSO if reionization is not (is) complete at  $z \gtrsim 6$ . Similarly, the ERM predicts peaks of width  $\sim 1\text{\AA}$  in 40 per cent of the lines of sight in the redshift range  $6.0 - 6.6$ ; in the same range, LRM predicts no peaks of width  $> 0.8\text{\AA}$ . We conclude that the dark gap and peak width statistics represent superb probes of cosmic reionization if about ten QSOs can be found at  $z > 6$ . We finally discuss strengths and limitations of our method.

**Key words:** intergalactic medium quasars: absorption lines - cosmology: theory large-scale structure of Universe.

## 1 INTRODUCTION

After the recombination epoch at  $z \sim 1100$ , the universe remained almost neutral until the first generation of luminous sources (stars, accreting black holes, etc) were formed. The photons from these sources ionized the surrounding neutral medium and once these individual ionized regions started overlapping, the global ionization and thermal state of the intergalactic gas changed drastically. This is known as the reionization of the universe, which has been an important subject of research over the last few years, especially because of its strong impact on the formation and evolution of the first cosmic structures (for a comprehensive review on the subject of reionization and first cosmic structures, see Ciardi & Ferrara 2005). Calculations based on the hierarchical structure formation in cold dark matter (CDM) models, predict that reionization should naturally occur somewhere between  $z \sim 6 - 15$  (Chiu & Ostriker 2000; Gnedin 2000).

Recent observational progresses, however, seem to indicate that the reionization history at high redshifts might have been a complicated process. To start with, WMAP observations of the temperature-polarization cross correlation at large scales for the CMB suggest a Thomson optical depth as high as  $\tau_e \sim 0.17$ , which

implies that reionization might have occurred at redshifts as high as  $z \sim 15$  (Kogut et al. 2003; Spergel et al. 2003). On the other hand, the spectroscopy of the Ly $\alpha$  forest for QSOs at  $z > 6$  discovered by the Sloan Digital Sky Survey (SDSS; Fan et al. 2001; Fan et al. 2003; Fan et al. 2005) seems to indicate that the ionization state of the intergalactic medium (IGM) might be very different along different lines of sight. For example, the analyses of the spectrum of the most distant known quasar (SDSS J1148+5251) show some residual flux both in the Ly $\alpha$  and Ly $\beta$  troughs, which when combined with Ly $\gamma$  region (Furlanetto & Oh 2005), imply that this flux is consistent with pure transmission. The presence of unabsorbed regions in the spectrum corresponds to a highly ionized IGM along that particular line of sight. However, Becker et al. (2001) detected a complete Gunn-Peterson trough in the spectrum of SDSS J1030+0524 ( $z = 6.28$ ), where no transmitted flux is detected over a large region ( $300\text{\AA}$ ) immediately blueward of the Ly $\alpha$  emission line. This result has been shown to be consistent with a hydrogen neutral fraction  $f_{\text{HI}} \gtrsim 10^{-3}$  (Fan et al. 2002, hereafter F02).

There have been other different approaches to investigate the neutral hydrogen fraction. Wyithe, Loeb, & Carilli (2005) and Wyithe & Loeb (2004) have estimated the sizes of the ionized regions around 7 QSOs at  $z > 6$  (which included the above cited QSO). Following that they considered the neutral gas surrounding the QSO as a function of different parameters: the Strömgren sphere size  $R_S$ , the quasar's production rate of ionizing photons

<sup>\*</sup> E-mail: galleran@sisssa.it

<sup>†</sup> E-mail: chou@sisssa.it

<sup>‡</sup> E-mail: ferrara@sisssa.it

$\dot{N}_{\text{phot}}$ , the clumping factor of the gas  $C$  and the age of the QSO  $t_{\text{age}}$ . According to their arguments, the small sizes of the HII regions ( $\sim 10$  physical Mpc) imply that the typical neutral hydrogen fraction of the IGM beyond  $z \sim 6$  is in the range 0.1 - 1. However, this approach is weighted down by several uncertainties. For example, one of the uncertainties is the quasar's production rate of ionizing photons  $\dot{N}_{\text{phot}}$  as it depends on the shape of the spectral template used. Moreover it is implicitly assumed in the modelling of clumping factor that the formation of quasars and galaxies were simultaneous. This in turn implies that quasars ionize only low density regions and hence the clumping factor which regulates the evolution of the HII regions is low. If, instead, stars appear much earlier than QSOs, the quasars have to ionize high density regions, which means that one should use a higher value of clumping factor in the calculations (Yu & Lu 2005).

Mesinger & Haiman (2004) have used a different approach based on the damping wings of the neutral hydrogen. Using density and velocity fields obtained by hydrodynamical simulation, they computed the Ly $\alpha$  absorption as a function of wavelength. In this case the neutral hydrogen fraction,  $\dot{N}_{\text{phot}}$  and  $R_S$  are treated as free parameters, constrained by matching the optical depth observed in the QSO SDSS J1030+0524. Also in this case they find a neutral hydrogen fraction larger than 10 per cent, i.e. the IGM is significantly more neutral at  $z \sim 6$  than the lower limit directly obtainable from the GP trough of the QSO spectrum ( $10^{-3}$ ). However this result is based only on one quasar. Moreover the observational constraints on the optical depth are very uncertain and can introduce errors in the estimates of  $f_{\text{HI}}$ .

The fact that we find transmission along some lines of sight while the medium seems quite neutral along others possibly has been interpreted that the IGM ionization properties are different along different lines of sight at  $z \gtrsim 6$ , thus suggesting that we might be observing the end of the reionization process.

Finally, the evolution of the luminosity function of Ly $\alpha$  emitters (Malhotra & Rhoads 2004; Furlanetto, Zaldarriaga, & Hernquist 2005; Haiman & Cen 2005) suggests that the neutral fraction of hydrogen at  $z = 6.5$  should be greater than 50 per cent (Malhotra & Rhoads 2005).

From a theoretical point of view several efforts have been made in the last few years in order to reconcile WMAP and SDSS measurements (e.g. Chiu et al. 2003; Haiman & Holder 2003; Gnedin 2004). In particular, Choudhury & Ferrara (2005, hereafter CF05) have showed that a self-consistent model for reionization, which agrees with various sets of observations over a wide redshift range, predicts a highly ionized universe at  $z \approx 6$ . According to the model, the rise in the GP optical depth towards  $z = 6$  is achieved by assuming a drop of the photoionization rate caused by the disappearance of first generation metal free (hereafter PopIII) stars. To explore this idea, it becomes important to verify whether the difference in the GP trough along different lines of sight at  $z > 6$  can be explained by assuming a highly ionized universe. In other words we pose the question: is it possible that the IGM is overall in a highly ionized state and the differences observed in QSO spectra arise simply due to the cosmic variance in density fluctuations?

Since at redshifts larger than 5, the transmission in the spectra is extremely low, the mean transmitted flux being  $F_{\text{mean}} \lesssim 0.182$  (Songaila 2004, hereafter S04), it is not possible to study the properties of the Ly $\alpha$  forest through the usual Voigt profile analysis. Alternative quantities have been used to characterize the spectra and to compare them with models, such as the probability distribution function (PDF) of the flux (F02; Songaila & Cowie 2002, hereafter SC02) and more importantly, the distribution of the dark

gap widths. It turns out that the length of dark gaps at high redshifts can be quite large ( $\sim 80$  Mpc comoving, which corresponds to  $\sim 30\text{\AA}$  in the rest frame wavelength at redshift 6), and hence the modelling requires a large sample of very long lines of sight (say,  $\gtrsim 100$  Mpc). Such requirement is beyond the reach of current numerical simulations and can only be fulfilled through semi-analytical calculations.

In this paper we use semi-analytical techniques to produce artificial spectra of the Ly $\alpha$  forest in the redshift range  $5.0 < z < 6.6$ . We have considered different reionization scenarios, namely, (i) an early reionization model (CF05), characterized by an highly ionized IGM for  $z \lesssim 14$ , and (ii) a late reionization model, in which the overlapping of ionized regions is completed only by  $z \sim 6$ . The main goal of this paper is to identify a statistics for the Ly $\alpha$  forest at  $z > 6$  which can be used as an effective tool for discriminating between the two scenarios above.

The outline of this paper is as follows. Section 2 presents the formalism to simulate the Ly $\alpha$  flux from the IGM density and peculiar velocity fields. In addition, we also describe the two reionization scenarios in detail. Section 3 contains the comparison of our models with observational data at  $z < 6$ . We introduce various statistical tools for the Ly $\alpha$  forest and use our models to make testable predictions for  $z \gtrsim 6$ . Finally we summarize our conclusions in Section 4.

## 2 SIMULATING THE QSO ABSORPTION SPECTRA

The Ly $\alpha$  forest, observed in the absorption spectra of distant quasars, is the result of photon absorption through Ly $\alpha$  transition of neutral hydrogen gas in the intergalactic medium along the line of sight (LOS). It is believed that the Ly $\alpha$  forest arises from low-amplitude fluctuations in the underlying baryonic density field (Bi, Börner & Chu 1992). In this work, we shall use the formalism developed by Bi & Davidsen (1997), Choudhury, Srianand, & Padmanabhan (2001) and Viel et al. (2002) to simulate random LOS realizations of the Ly $\alpha$  forest as observed in the quasar absorption spectra.

### 2.1 Neutral hydrogen density and the transmitted flux

Let us first summarize the steps for calculating the neutral hydrogen density field, optical depth and the transmitted flux for the Ly $\alpha$  forest:

#### 2.1.1 Linear density and velocity fields for baryons

In the linear regime, both the density and velocity fields for baryons are gaussian and are completely determined by the corresponding power spectra and correlation functions. The linear density power spectrum for baryons in one dimension is given by

$$P_b^{(1)}(k, z) = \frac{D^2(z)}{2\pi} \int_k^\infty dq q W_b^2(q, z) P_{\text{DM}}^{(3)}(q) \quad (1)$$

where  $P_{\text{DM}}^{(3)}(k)$  is the dark matter power spectrum in three dimensions at redshift  $z = 0$ ,  $D(z)$  is the growth factor of linear DM density fluctuations [normalized so that  $D(z = 0) = 1$ ] and  $W_b(k, z)$  is the low-pass filter which suppresses baryonic fluctuations at small scales. It is well known that the exact form of  $W_b(k, z)$  depends on the ionization and thermal history of the universe, and one should, in principle, couple the evolution of the baryonic fluctuations to the reionization history. Since this is computationally

quite complex, one is led to use various approximate forms for the filter function. It turns out that if the temperature of the IGM is smoothly increasing with redshift and does not undergo any abrupt change (which is the case for our models), the filter function can be assumed to be of the form

$$W_b(k, z) = \frac{1}{1 + x_b^2(z)k^2} \quad (2)$$

where  $x_b(z)$  denotes the comoving scale below which fluctuations are suppressed:

$$x_b(z) = \frac{1}{H_0} \left[ \frac{2\gamma k_B T_m(z)}{3\mu m_p \Omega_m (1+z)} \right]^{1/2}. \quad (3)$$

The constant  $\mu$  is the mean molecular weight of the IGM, given by  $\mu = 2/(4 - 3Y)$ , where  $Y = 0.24$  is the helium mass fraction (this relation assumes that the IGM consist mostly of fully ionized hydrogen and singly ionized helium). In equation (3)  $k_B$  is the Boltzmann constant,  $m_p$  is the hydrogen mass,  $\Omega_m$  is the density parameter for non-relativistic matter,  $T_m$  is the mass-averaged temperature and  $\gamma$  is the ratio of specific heats. Note that we are using the mass-averaged temperature  $T_m$  which is considerably higher than the conventionally used temperature at the mean gas density  $T_0$ . This is motivated by the fact that baryonic density fluctuations calculated using the mass-averaged temperature are in a much better agreement with the results of numerical simulations. The evolution of  $T_m$  with  $z$  has been computed as described in CF05, in Section 5.

The CDM power spectrum in three dimensions is taken to be  $P_{\text{DM}}^{(3)}(k) = A_{\text{DM}} k^n T_{\text{DM}}^2(q)$ , where  $n$  is the spectral index and  $T_{\text{DM}}(q)$  is the CDM transfer function (Bardeen et al. 1986):

$$T_{\text{DM}}(q) = \frac{\ln(1 + 2.34q)}{2.34q} \times \left[ 1 + 3.89q + (16.1q)^2 + (5.46q)^3 + (6.71q)^4 \right]^{-1/4}, \quad (4)$$

with  $q \equiv k/(h \text{ Mpc}^{-1})\Gamma^{-1}$ . The shape parameter  $\Gamma$  depends on the Hubble parameter,  $\Omega_m$  and  $\Omega_b$  (Sugiyama 1995):

$$\Gamma = \Omega_m h \exp \left[ -\Omega_b \left( 1 + \frac{\sqrt{2h}}{\Omega_m} \right) \right]. \quad (5)$$

The normalization parameter  $A_{\text{DM}}$  is fixed through the value of  $\sigma_8$  (the rms density fluctuations in spheres of radius  $8 h^{-1} \text{ Mpc}$ ).

The computation of the linear baryonic peculiar velocity field  $v_{\text{pec}}(x, z)$  is similar to that for the density field. We use the linear power spectrum for the velocity field in one dimension given by

$$P_v^{(1)}(k, z) = \left[ \frac{\dot{D}(z)}{1+z} \right]^2 k^2 \frac{1}{2\pi} \int_k^\infty \frac{dq}{q^3} W_b^2(q, z) P_{\text{DM}}^{(3)}(q) \quad (6)$$

In addition, we do take into account the fact that the velocity field is correlated with the density field

$$P_{bv}^{(1)}(k, z) = \frac{\dot{D}(z)}{1+z} k \frac{1}{2\pi} \int_k^\infty \frac{dq}{q} W_b^2(q, z) P_{\text{DM}}^{(3)}(q). \quad (7)$$

Given the above relations and using the properties of gaussian random fields, one can generate the density and peculiar velocity fields for baryons in the linear regime. These are discussed in details in Bi & Davidsen (1997), Choudhury, Srianand, & Padmanabhan (2001) and Viel et al. (2002).

### 2.1.2 Quasi-linear density field for baryons

The above analysis is done in the framework of linear perturbation theory, while to study the properties of the IGM one has to take into account nonlinearities in the density distribution. To generate the mildly non-linear regime of the IGM local density we use a lognormal model, introduced by Coles & Jones (1991) for the nonlinear matter distribution in the universe and widely adopted later (Bi 1993; Bi & Davidsen 1997; Choudhury, Padmanabhan, & Srianand 2001; Choudhury, Srianand, & Padmanabhan 2001; Viel et al. 2002) for the case of IGM. The lognormal distribution of the baryonic density field is given by

$$n_b(x, z) = n_0(z) \exp \left[ \delta_b(x, z) - \frac{\langle \delta_b(x, z) \rangle^2}{2} \right] \quad (8)$$

where  $\delta_b$  is the linear baryonic density contrast and  $n_0(z)$  is the mean IGM density which is related to the baryonic density parameter  $\Omega_b$  and the critical density  $\rho_c$  through the relation

$$n_0(z) = \frac{\Omega_b \rho_c}{\mu m_p} (1+z)^3. \quad (9)$$

We should mention here that the lognormal model is found to under-predict the number of high density regions compared to what is found in numerical simulations (CF05), and hence is inadequate for describing the highly non-linear densities. However, since these high density regions are quite rare, we expect them to have little effect on the statistics of Ly $\alpha$  forest performed in this paper. Thus, as far as this work is concerned, the lognormal approximation should work reasonably well for studying the properties of Ly $\alpha$  forest. The accuracy of the lognormal approximation has been validated by Choudhury, Srianand, & Padmanabhan (2001) and CF05; the model is able to match various sets of observations simultaneously over a wide range of redshifts. For the purpose of this paper, we have also carried out some additional comparisons of the lognormal model with HydroPM simulations (Gnedin & Hui 1998) and found that, as far as the flux statistics used in this paper (the PDF and the distribution of dark gap widths) are concerned, the model gives quite good agreement with simulations. The details of such comparisons are given in Appendix A.

### 2.1.3 Neutral hydrogen distribution

The low density gas which gives rise to the Ly $\alpha$  forest is approximately in local equilibrium between photoionization and recombination, expressed by the relation

$$\alpha[T(x, z)] n_p(x, z) n_e(x, z) = \Gamma_{\text{HI}}(x, z) n_{\text{HI}}(x, z) \quad (10)$$

where  $\alpha(T)$  is the radiative recombination rate,  $n_e$  and  $n_p$  are the number density of electrons and protons respectively and  $\Gamma_{\text{HI}}$  is the photoionization rate of neutral hydrogen. The characteristic low density of the IGM allow us to neglect the collisional ionizations.

It is useful to define the neutral hydrogen fraction  $f_{\text{HI}}$ :

$$f_{\text{HI}}(x, z) \equiv \frac{n_{\text{HI}}(x, z)}{n_{\text{H}}(x, z)} = 1.08 \frac{n_{\text{HI}}(x, z)}{n_b(x, z)}. \quad (11)$$

where the factor 1.08 arises because of the presence of helium. To solve the ionization equilibrium equation (10) in an exact manner we need to know the precise ionization state of helium (which affects the number density of electrons  $n_e$ ). However we can obtain the neutral fraction in the two extreme cases which are discussed next. Usually, the ionization conditions in the Ly $\alpha$  forest at  $3.5 < z < 5.5$  are similar to those of HII regions with  $f_{\text{HI}} \lesssim 10^{-4}$ ;

furthermore in such epochs, helium is mostly in a singly-ionized state. Thus with the approximation  $f_{\text{HI}} \ll 1$ , equation (10) gives

$$f_{\text{HI}}(x, z) \approx 1.08 \frac{\alpha[T(x, z)]}{\Gamma_{\text{HI}}(x, z)} n_{\text{H}}(x, z) = \frac{\alpha[T(x, z)]}{\Gamma_{\text{HI}}(x, z)} n_b(x, z). \quad (12)$$

However, at higher redshifts (say,  $z > 5.5$ ), one has to consider the possibility that the IGM is not completely ionized and there remain regions with a high neutral fraction. Such regions are opaque to ionizing radiation, and hence the effective photoionization rate in such regions can be taken to be zero; it follows that  $f_{\text{HI}} \approx 1$ .

The recombination coefficient at temperature  $T$  is given by (Rauch et al. 1997)

$$\alpha[T(x, z)] = 4.2 \times 10^{-13} \left[ \frac{T(x, z)}{10^4 K} \right]^{-0.7} \text{ cm}^3 \text{ s}^{-1} \quad (13)$$

For quasi-linear IGM, where non-linear effects like shock-heating can be neglected, the temperature  $T(x, z)$  can be related to the baryonic density through a power-law relation (Hui & Gnedin 1997; Schaye et al. 2000)

$$T(x, z) = T_0(z) \left[ \frac{n_b(x, z)}{n_0(z)} \right]^{\gamma-1} \quad (14)$$

where  $T_0(z)$  is the temperature of the IGM at the mean density.

The slope  $\gamma$  of the equation of state depends on the reionization history of the universe (Theuns et al. 1998; Hui & Gnedin 1997). The value of  $\gamma$  and its evolution are still quite uncertain and hence in this work we will consider it as a free parameter and ignore its redshift evolution.

#### 2.1.4 Optical depth and transmitted flux for the Ly $\alpha$ forest

The transmitted flux  $F$  due to Ly $\alpha$  absorption in the IGM is computed from the usual relation  $F = e^{-\tau_{\text{Ly}\alpha}}$ , where  $\tau_{\text{Ly}\alpha}$  is the Ly $\alpha$  absorption optical depth. The value of the optical depth at a redshift  $z_0$  is given by

$$\tau_{\text{Ly}\alpha}(z_0) = \frac{cI_\alpha}{\sqrt{\pi}} \int dx(z) \frac{n_{\text{HI}}(x(z), z)}{b(x(z), z)(1+z)} \times V \left[ \alpha, \frac{v_H(z_0) - v_H(z) - v_{\text{pec}}(x(z), z)}{b(x(z), z)} \right], \quad (15)$$

where  $v_H(z_0) - v_H(z) = c(z_0 - z)/(1 + z_0)$  denotes the differential Hubble velocity between two points along the LOS. The quantity  $I_\alpha = 4.45 \times 10^{-18} \text{ cm}^2$ ,

$$b(x, z) = \left[ \frac{2k_B T(x, z)}{m_p} \right]^{1/2} \quad (16)$$

is the Doppler parameter,  $V$  is the Voigt function and  $\alpha$  measures the natural line width of Ly $\alpha$  transition. The quantity  $x(z)$  denotes the comoving distance to a point along the LOS at a redshift  $z$ :

$$x(z) = \int_0^z dz' \frac{c}{H(z')} \quad (17)$$

In this work, each LOS is discretized in a number of pixels  $N_{\text{pix}}$ . At each pixel, we calculate the neutral hydrogen density  $n_{\text{HI}}$  and the peculiar velocity  $v_{\text{pec}}$  through the procedure discussed above. Then the optical depth at a pixel  $i$  is given by

$$\tau_{\text{Ly}\alpha}(i) = cI_\alpha \frac{\Delta x}{1+z} \sum_{j=1}^{N_{\text{pix}}} n_{\text{HI}}(j) \Phi_\alpha[v_H(i) - v(j)] \quad (18)$$

where  $\Delta x$  is the comoving pixel size,  $v(i) = v_H(i) + v_{\text{pec}}(i)$  is the total velocity in the pixel  $i$  and  $\Phi_\alpha$  is the Voigt profile for Ly $\alpha$

transition. For low column density regions, the natural broadening is not that important, and the Voigt function reduces to a simple Gaussian

$$\Phi_\alpha[v_H(i) - v(j)] = \frac{1}{\sqrt{\pi} b(j)} \exp \left[ - \left( \frac{v_H(i) - v(j)}{b(j)} \right)^2 \right]. \quad (19)$$

However, one should keep in mind that while dealing with highly neutral regions (which is relevant for the late reionization scenario), the Gaussian approximation for the line profile is not valid, and one has to use the appropriate form for the Voigt profile. In regions away from the center, the profile is given by the Lorentzian form:

$$\Phi_\alpha[v_H(i) - v(j)] = \frac{R_\alpha}{\pi[(v_H(i) - v(j))^2 + R_\alpha^2]} \quad (20)$$

where  $R_\alpha \equiv \Lambda_\alpha \lambda_\alpha / 4\pi$  with  $\Lambda_\alpha$  being the decay constant for the Ly $\alpha$  resonance and  $\lambda_\alpha$  is the wavelength of the Ly $\alpha$  line.

Similar expressions follow for Ly $\beta$  absorption lines too. In particular equation (18) is replaced by

$$\tau_{\text{Ly}\beta}(i) = cI_\beta \frac{\Delta x}{1+z} \sum_{j=1}^{N_{\text{pix}}} n_{\text{HI}}(j) \Phi_\beta[v_H(i) - v(j)] \quad (21)$$

where  $I_\beta = (f_{\text{Ly}\beta} \lambda_{\text{Ly}\beta}) / (f_{\text{Ly}\alpha} \lambda_{\text{Ly}\alpha}) I_\alpha$ , with  $(f_{\text{Ly}\beta} \lambda_{\text{Ly}\beta}) / (f_{\text{Ly}\alpha} \lambda_{\text{Ly}\alpha}) = 0.16$  being the ratio of the product between the oscillator strength and the resonant scattering wavelength for Ly $\beta$  and Ly $\alpha$ ;  $\Phi_\beta$  is the Voigt profile for Ly $\beta$  transition. For low column density systems,  $\Phi_\beta$  has the Gaussian form and it is essentially the same as  $\Phi_\alpha$ . Hence, for such systems, we have  $\tau_{\text{Ly}\beta}(i) = 0.16 \tau_{\text{Ly}\alpha}(i)$ . However, the situation is different for highly neutral regions, where  $\Phi_\beta$  depends on the decay constant for the resonance line and thus is different from  $\Phi_\alpha$ . In particular, for regions away from the center, the profile is of the Lorentzian form:

$$\Phi_\beta[v_H(i) - v(j)] = \frac{R_\beta}{\pi[(v_H(i) - v(j))^2 + R_\beta^2]} \quad (22)$$

where  $R_\beta \equiv \Lambda_\beta \lambda_\beta / 4\pi$ .

#### 2.1.5 Simulation of observational and instrumental effects

In this work, we compute various statistical quantities related to the Ly $\alpha$  forest using our simulated spectra, such as (i) the evolution of the Gunn-Peterson optical depth ( $\tau_{\text{GP}}$ ), (ii) the Probability Distribution Function (PDF) and (iii) the Dark Gap Width Distribution (DGWD), which can then be compared with observational results. To make sure that the simulated spectra contain the same artifacts as the observed ones, we take into account the broadening of lines due to instrumental profile, the pixel size and noise. In this regard, we first convolve each simulated spectra with a Gaussian with a Full Width at Half Maximum (FWHM) corresponding to the resolution of the instrument used for observations. We then re-sample each line to varying pixel size. We finally add noise to the simulated Ly $\alpha$  forest spectra corresponding to the observed data in a manner that the flux  $F$  in each pixel is replaced by  $F \rightarrow F + \sigma_{\text{noise}} G(1)$ , where  $\sigma_{\text{noise}} = 0.02$  and  $G(1)$  is a Gaussian random deviate with zero mean and unit variance. We have also studied the effect of varying the FWHM, the pixel size and  $\sigma_{\text{noise}}$  on different statistical quantities and shall comment on them wherever appropriate.

## 2.2 Reionization models

As it is clear from the above discussion, the simulation of the Ly $\alpha$  forest spectra requires the knowledge of a few free param-

ters. For the background cosmological model and the CDM power spectrum, we use the best-fit values given by WMAP experiment<sup>1</sup>. This leaves us with the parameters related to the IGM, which are  $T_m(z)$ ,  $T_0(z)$ ,  $\Gamma_{\text{HI}}(x, z)$  and  $\gamma(z)$ . One approach could be to treat them as free parameters and try to constrain them by comparison with observations. However, the evolution of all the above parameters depends on the detailed ionization and thermal history of the IGM and can be quite complex – hence constraining the parameters over a wide redshift range is not straightforward. The other approach is to use a self-consistent model for thermal and ionization history of the universe and calculate the globally-averaged values of the above quantities.

In this paper, we take the second approach and use the semi-analytical model of CF05 to obtain the globally-averaged values of  $T_m$ ,  $T_0$ ,  $\Gamma_{\text{HI}}$  at different redshifts. The model implements most of the relevant physics governing the thermal and ionization history of the IGM, such as the inhomogeneous IGM density distribution, three different classes of ionizing photon sources (massive PopIII stars, PopII stars and QSOs), and radiative feedback inhibiting star formation in low-mass galaxies. The main advantage of the model is that its parameters can be constrained quite well by comparing its predictions with various observational data, namely, the redshift evolution of Lyman-limit absorption systems (Storrie-Lombardi et al. 1994), Gunn-Peterson (Songaila 2004) and electron scattering optical depths (Kogut et al. 2003), temperature of the IGM (Schaye et al. 1999) and cosmic star formation history (Nagamine et al. 2004).

According to the above model, the redshift of reionization is identified with the onset of the post-overlap stage (Gnedin 2000), which is defined as the epoch where the volume filling factor of ionized hydrogen in low-density regions (with overdensities less than a few tens) reaches unity ( $Q_{\text{HII}} = 1$ ). Following this, the ionized regions start propagating into the neutral high density regions, which is manifested as the evolution in the specific number of Lyman-limit systems. In what follows we will consider two different reionization scenarios:

#### Early Reionization Model (ERM)

This model, which refers to the fiducial model described in CF05, is characterized by an highly ionized IGM at redshifts  $z \lesssim 14$ . In this scenario, an early population of massive metal-free (PopIII) stars ionize hydrogen at high redshifts, thus producing the high electron scattering optical depth observed by WMAP. The PopIII stars start disappearing at  $z_{\text{trans}} \approx 10$ ; at lower redshifts, PopII stars and QSOs contribute to the ionizing background with a large number of photons with energies above 13.6 eV which are able to maintain the ionized state of hydrogen. In this model we assume the photoionization rate to be spatially homogeneous and equal to the globally averaged value, i.e.,  $\Gamma_{\text{HI}}(x, z) \equiv \Gamma_{\text{HI}}(z)$ .

In the context of the present work, where we are concerned with state of the IGM at  $5.5 \lesssim z \lesssim 6.5$ , the ERM corresponds to a highly ionized IGM at these redshifts. While it is true that this model can explain a large number of observational constraints, it is in contradiction with the analyses predicting that the IGM could be in a highly neutral state at  $z \gtrsim 6$  (Wyithe, Loeb, & Carilli 2005;

Wyithe & Loeb 2004; Mesinger & Haiman 2004). Hence it becomes necessary to consider an alternative model for reionization where the IGM is predominantly neutral at  $z \gtrsim 6$ .

#### Late Reionization Model (LRM)

The main motivation to consider this model is to verify whether the Ly $\alpha$  forest can still be used to determine the ionization state of the IGM at  $z \gtrsim 6$ . In this model, the hydrogen distribution in the low-density IGM is characterized by two distinct phases at  $z \gtrsim 6$ , namely an ionized (HII) phase with a volume filling factor  $Q_{\text{HII}}$  and a neutral (HI) phase with a volume filling factor  $1 - Q_{\text{HII}}$ , with the evolution of  $Q_{\text{HII}}$  and other physical parameters, [ $T_m(z)$ ,  $T_0(z)$ ,  $\Gamma_{\text{HI}}(z)$ ] being calculated self-consistently using the model of CF05. To achieve this two-phased state, we consider an ionizing background different from ERM one. In fact, the main (and only) difference between ERM and LRM is that the PopIII stars do not play an efficient role for reionization in LRM and as a consequence the IGM remains neutral up to redshift 6, until the contribution of PopII stars to the UV background starts becoming substantial. In passing, we should mention that in the ERM the electron scattering optical depth is  $\tau_e = 0.17$ , in perfect agreement with the high value measured by WMAP, while in the LRM it is  $\tau_e = 0.06$ , value which is lower than the  $2\sigma$  limit allowed by WMAP.

#### Model comparison

To compare the global properties of the two reionization models, we plot the evolution of the volume filling factor of ionized regions  $Q_{\text{HII}}(z)$  in the left panel of Figure 1. It is clear that the two models differ only at  $z > 6$ ; for the LRM  $Q_{\text{HII}}$  evolves from 0.7 to unity in the redshift range 6.6–6.0, implying that the universe is in the pre-overlap stage, while for the ERM,  $Q_{\text{HII}} = 1$  at these epochs.

We next compare the evolution of the globally volume-averaged photoionization rate for the two models in the middle panel of Figure 1. At  $z < 6$  the ionizing sources are mainly PopII stars and QSOs for both models and so  $\Gamma_{\text{HI}}$  is comparable in the two models. At  $z > 6$ , there are no contributions from PopIII stars to the UV background radiation in the LRM, which are instead present in the ERM. As a consequence, at high redshift,  $\Gamma_{\text{HI}}$  is higher in the ERM with respect to the late reionization one. The photoionization rate evolution is also compared with the results obtained by F02 and Bolton et al. (2005), hereafter B05. The agreement is quite good with B05 data at  $z \leq 4$ ; the mild discrepancy at  $z \approx 4$  could be attributed to the systematic overestimation of the photoionization rate due to the limited box size and resolution of their hydrodynamical simulations. On the other hand, the ERM mildly violates the upper limit of  $\Gamma_{\text{HI}} = 0.08$  at  $z = 6.0$  obtained by F02. However F02 use  $\Gamma_{\text{HI}}$  as a free parameter (same as in B05) to match the mean transmitted flux at high redshift, whose value has a large uncertainty (see Section 3.1.1). So we expect that also the values of  $\Gamma_{\text{HI}}$  at  $z > 4$  are associated with uncertainties at least as large as for the estimates at lower redshifts. This alleviates the mild discrepancy between the ERM and the upper limit on  $\Gamma_{\text{HI}}$  suggested by F02 at  $z = 6$ .

The globally volume averaged neutral hydrogen fraction  $f_{\text{HI}}$  is shown in the right panel of Figure 1. The evolution of  $f_{\text{HI}}$  with redshift has been obtained computing 10 LOS for eight redshift bins ( $\Delta z = 0.4$ ) covering the redshift interval 2.8–6.7. Figure 1 shows that, as expected, the IGM is highly ionized for the ERM, while it is quite neutral at  $z \gtrsim 6$  for the LRM. Furthermore, and opposite to the ERM case, we find a sharp evolution in the neutral fraction around  $5.5 < z < 6.5$  for the LRM when overlapping occurs in that model. Our prediction on the neutral hydrogen fraction

<sup>1</sup> Throughout this paper we will assume a flat universe with total matter, vacuum, and baryonic densities in units of the critical density of  $\Omega_m = 0.27$ ,  $\Omega_\Lambda = 0.73$ , and  $\Omega_b h^2 = 0.024$ , respectively, and a Hubble constant of  $H_0 = 100h \text{ km s}^{-1} \text{ Mpc}^{-1}$ , with  $h = 0.72$ . The parameters defining the linear dark matter power spectrum are  $\sigma_8 = 0.9$ ,  $n = 0.99$ ,  $dn/d \ln k = 0$ .

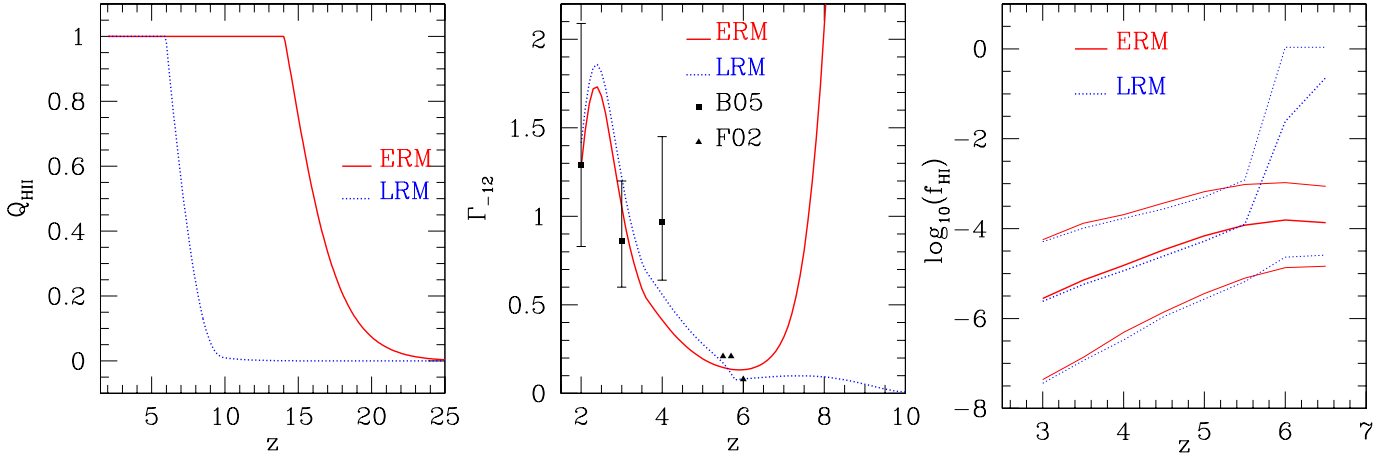


**Figure 1.** Evolution of the volume filling factor of ionized regions (left), the globally volume-averaged photoionization rate in units of  $10^{-12}\text{s}^{-1}$ ,  $\Gamma_{-12} = \Gamma_{\text{HI}}/10^{-12}\text{s}^{-1}$  (middle) and the neutral hydrogen fraction (right) for the early (ERM) and late (LRM) reionization models. The points in the middle panel show results obtained by Bolton et al. (2005) (B05, filled squares) and Fan et al. (2002) (F02, filled triangles) using hydrodynamical and N-body simulations, respectively. In the right panel, thick lines represent average results over 10 LOS, while the thin lines denote the upper and lower neutral hydrogen fraction extremes in each redshift interval.

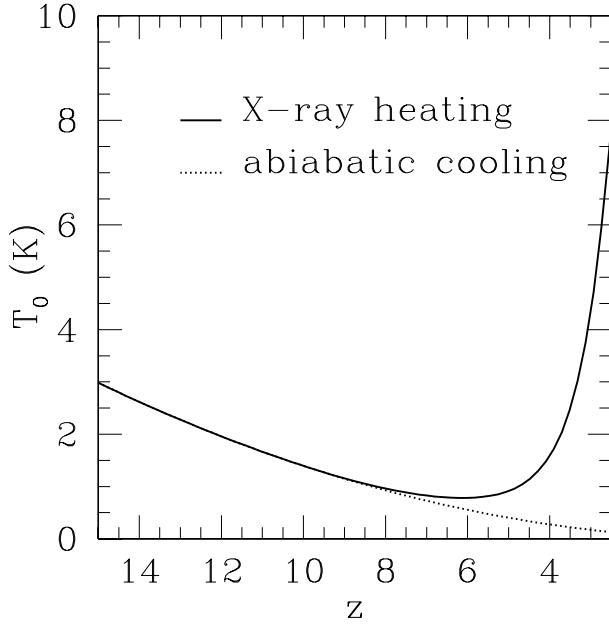


**Figure 2.** Temperature evolution of the neutral regions. The solid line refers to the model with X-ray heating described in the text; the dotted line describes the temperature evolution assuming adiabatic cooling.

at  $z = 6$ , considering cosmic variance, is in agreement with the result obtained by F02, while there is a discrepancy with the measure of  $f_{\text{HI}}$  arising from the analyses of the HII regions (Wyithe, Loeb, & Carilli 2005; Wyithe & Loeb 2004; Mesinger & Haiman 2004) as discussed in the Introduction.

### 2.3 Additional physics

In the two-phase model, the photoionization rate  $\Gamma_{\text{HI}}$  is nearly zero in the neutral HI regions, as most of the points are opaque to ionizing radiation. On the other hand, the photoionization rate  $\Gamma_{\text{HI}}^{\text{HII}}(z)$  inside HII regions is assumed to be homogeneous; a natural way

to relate it to the globally volume-averaged photoionization rate  $\Gamma_{\text{HI}}(z)$  is through the relation:  $\Gamma_{\text{HI}}^{\text{HII}}(z) = \Gamma_{\text{HI}}(z)/Q_{\text{HII}}(z)$ .

Also to be noted is that in absence of ionizing radiation, the temperature  $T_0$  of the mean density neutral gas will decrease adiabatically and can be as low as  $\sim 1$  K at  $z \approx 6$ ; however, the presence of a population of hard photons (say, soft X-ray photons from QSOs, X-ray binaries or supernova remnants), which are able to penetrate the atomic medium, can raise  $T_0$  for these neutral regions (Chen & Miralda-Escudé 2004). To investigate this possibility we study the evolution of  $T_0$  for neutral regions in the expanding Universe, integrating the following equation:

$$(1+z) \frac{dT_0}{dz} = 2T_0 - \frac{2}{3} \frac{\Gamma_{\text{tot}} - \Lambda_{\text{tot}}}{H(z)n_b k_B} \quad (23)$$

where  $\Gamma_{\text{tot}}$  and  $\Lambda_{\text{tot}}$  are the total heating and cooling rates, respectively. Assuming that the main heating mechanism is due to soft X-ray photons,  $\Gamma_{\text{tot}}$  can be substituted by  $\Gamma_X$ , where  $\Gamma_X$  is the X-ray heating rate. Following Chen & Miralda-Escudé (2004), we parametrize the emissivity in X-rays in terms of the fraction of energy that is emitted in X-rays compared to the energy emitted at Ly $\alpha$  per unit  $\log \nu$ , which we designate as  $\alpha_X$ . The X-ray heating rate is then given by the following relation:

$$\Gamma_X(z) = 0.14 \alpha_X h_P \nu_\alpha \epsilon(z) \quad (24)$$

where 0.14 is the fraction of the X-ray energy used to heat the gas (Shull & van Steenberg 1985),  $h_P$  is the Planck constant,  $\nu_\alpha$  is the frequency of the Ly $\alpha$  transition and  $\epsilon$  is the comoving Ly $\alpha$  emissivity as obtained in the LRM.

We start solving the differential equation (24) from  $z_{\text{start}} = 30$  assuming that, at this redshift  $\epsilon(z) \approx 0$ . In the absence of any heating sources, the temperature of the gas can be shown to be  $\sim 11$  K.<sup>2</sup> During the redshift range covered in the calculation, the

<sup>2</sup> The Compton scattering between the CMB photons and relic free electrons from cosmic recombination couples the cosmic gas temperature to the CMB one, down to redshift  $1 + z_f \sim 1000(\Omega_b h^2)^{2/5}$  (Peebles 1993). Following that the temperature of the gas cools down adiabatically. So the gas temperature before the formation of any heating source is given by

temperature of the gas is low enough to neglect cooling as the cooling function is different from zero only for temperatures above  $10^4$  K.

Figure (2) shows the thermal evolution for neutral regions when we include X-ray heating with  $\alpha_X = 0.01$ . Assuming that only 1 per cent of the energy is emitted as X-rays, the temperature of the gas is equal to 0.76 K at  $z = 6$ . Even when we use a higher value of  $\alpha_X = 0.1$ , the temperature raises only to 2.8 K at  $z = 6$ .

Fortunately for this work, it turns out that *all* the results are independent of the precise value of  $T_0$  for neutral regions as long as it is below 1500 K, with variations being less than the typical statistical variance. The reason for the insensitivity of our results to  $T_0$  can be understood in the following way: the value of  $T_0$  has two possible effects on the simulated spectra. The first effect is to determine the recombination rate of the ionized species and thus affect the neutral hydrogen fraction. However, the low ionization rates in the neutral regions imply very small ionized fraction and thus a very long recombination time, thus making the value of  $T_0$  irrelevant for calculating the neutral fraction. The second effect of  $T_0$  is to determine the widths of the lines through the Doppler profile. But here again, because of the large neutral fractions, the line profile is predominantly determined by the natural width (which shall be discussed in detail later) and thus the effect of  $T_0$  is again negligible. For the rest of the paper, we shall assume that the temperature  $T_0$  for neutral regions is 1K.

There are few more subtleties which need to be addressed while dealing with neutral regions along lines of sight. First, the volume filling factor  $Q_{\text{HII}}(z)$  applies to three dimensional regions only, and hence one needs to translate this into a one dimensional filling factor  $q_{\text{HII}}(z)$  along different lines of sight in a consistent manner which takes into account the evolution in  $Q_{\text{HII}}$ . This is a purely geometrical exercise and can be performed if one knows the geometry of the neutral regions. However, the value of the filling factor  $Q_{\text{HII}}$  does not uniquely determine the size and shape of the neutral regions; the detailed topology depends on the nature of sources, coupled with the density distribution of the IGM, and hence is non-trivial to take it into account analytically. On the other hand, numerical simulations still do not have enough dynamic range to address this issue for wide regions of parameter space. Given this, we devise an approximate method, described below, to calculate  $q_{\text{HII}}(z)$  along different lines of sight. In addition, we also study different variations of our method accounting for different topologies of the neutral regions, and check whether our main conclusions remain unchanged.

The simplest method of distributing the neutral regions along different lines of sight is based on the assumption that the positions of the neutral regions in the three-dimensions are completely random and the regions are *not* correlated with the density field. This assumption seems to be quite reasonable at late stages of reionization as found in radiative transfer simulations, where most of the individual ionized regions have overlapped leaving neutral regions of random shapes and sizes with no significant clustering pattern. (For a visual impression see, for example, the maps in Ciardi, Ferrara, & White 2003.) Of course, very high density regions, like collapsed structures or filaments, tend to remain neutral till late times, thus correlating the neutral regions with density field. However, these high density regions are not significant for the  $\text{Ly}\alpha$  forest, and hence can be ignored in our analysis. Nevertheless, we do check the

effects of clustering of neutral regions of large sizes and their correlation with the density field in Section 3.7. In addition we present the technical details of distributing the neutral regions along lines of sight and their physical properties in Appendix B.

### 3 RESULTS

In this Section, we present the main results of our analysis. In the first part, we shall put our model to test by comparing it with various available observations at  $z < 6$ . As we shall see, the model is quite successful in matching the observational data. Next, we shall discuss the predictions of the model at  $z > 6$  in the second part, and then try to determine the ionization state of the IGM.

#### 3.1 Comparison of the model with observations at $z < 6$

##### 3.1.1 Gunn-Peterson optical depth ( $\tau_{\text{GP}}$ )

The first obvious test for our model would be to check whether it can match the mean GP opacity of the  $\text{Ly}\alpha$  and  $\text{Ly}\beta$  forests at  $z < 6$ . For this purpose, we use the data from S04, and thus the procedure for obtaining the mean transmitted flux from simulated spectra is similar to that work. We consider the emission redshifts of the 50 QSOs observed ( $2.31 < z_{\text{em}} < 6.39$ ) as mentioned in Tables 1 and 2 in S04. For each emission redshift, we simulate the  $\text{Ly}\alpha$  absorption spectra covering the wavelength range 1080 - 1185 Å. We then divide each spectra in seven parts of length 15 Å and compute the  $\text{Ly}\alpha$  Mean Transmitted Flux (MTF) for each part. These data points are then binned in a way such that each bin contains six points. For each bin, the mean transmission and the extremes of transmission have been computed and then assigned to the median redshift within the bin. The GP optical depth is defined as:  $\tau_{\text{GP}} = -\ln(\text{MTF})$ . The GP optical depth evolution for  $\text{Ly}\alpha$  transition is plotted in Figure 3 (left panel) as a function of the median redshift in each bin. The vertical error bars show the range of extremes of transmission within each bin, weighted on 100 LOS, translated to optical depth.

In order to compare our results with observational ones (S04), each spectra have been convolved with a Gaussian whose FWHM is equal to  $8 \text{ km s}^{-1}$ , if the emission redshift  $z_{\text{em}}$  is below 4, or equal to  $56 \text{ km s}^{-1}$ , if  $z_{\text{em}} > 4$ . This procedure implies, in the first case, a resolution around 36000, since the observed spectra have been taken with the HIRES spectrograph on the Keck I telescope, while in the second case the mimicked resolution is 5300, the same of the ESI spectrograph on the Keck II telescope. The pixel size of the rebinning is  $12 \text{ km s}^{-1}$ .

Extending the above procedure for  $\text{Ly}\beta$  region of the absorption spectra (corresponding to the rest wavelength range 980 - 1010 Å), we derive the *total* optical depth at a given redshift  $z$  from the sum of the direct  $\text{Ly}\beta$  absorption at that redshift and the  $\text{Ly}\alpha$  absorption at redshift  $1 + z_\beta = \frac{\lambda_\beta}{\lambda_\alpha}(1 + z)$ , i.e.,

$$\tau_{\text{Ly}\beta}^{\text{tot}}(z) = \tau_{\text{Ly}\beta}(z) + \tau_{\text{Ly}\alpha}(z_\beta), \quad (25)$$

where  $\tau_{\text{Ly}\alpha}$  and  $\tau_{\text{Ly}\beta}$  are given by equations (18) and (21) respectively. For each emission redshift, the absorption spectra in the wavelength range 980 - 1010 Å is divided in two parts of 30 Å each. As in the  $\text{Ly}\alpha$ , we obtain the evolution of  $\text{Ly}\beta$  MTF and the range of extreme values by binning the data. Note that, in order to calculate the  $\text{Ly}\beta$  flux distribution in the rest wavelength range 980 - 1010 Å (as discussed above), we need to estimate the  $\text{Ly}\alpha$  optical depth in the interval 827 - 1010 Å [this follows trivially from the

$T_0(z_{\text{start}}) = T_{\text{CMB}}(1 + z_f) [(1 + z_{\text{start}})/(1 + z_f)]^2$ , where  $T_{\text{CMB}}$  is the temperature of the CMB at  $z = 0$ .

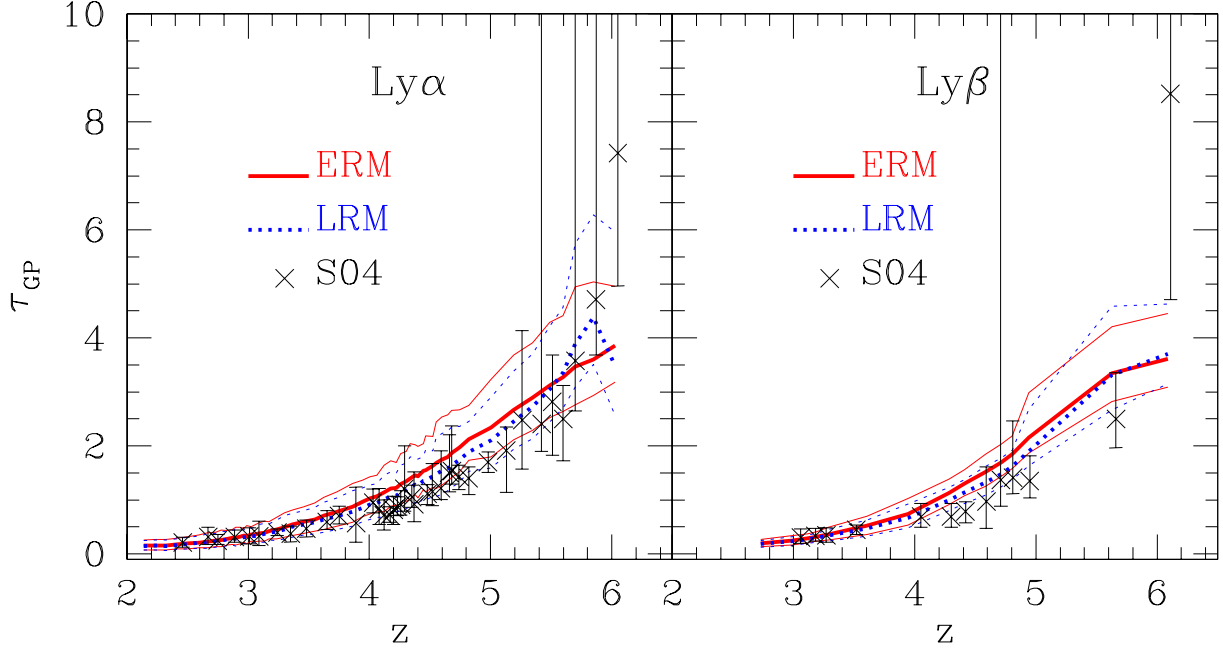


**Figure 3.**  $\text{Ly}\alpha$  (left panel) and  $\text{Ly}\beta$  (right panel) GP optical depth compared with data from Songaila (2004). Solid (red) and dotted (blue) thick lines represent average results for ERM and LRM, respectively, on 100 LOS for each emission redshift; the thin lines denote the upper and lower transmission extremes in each bin, weighted on 100 LOS.

expression (25) for  $\text{Ly}\beta$  optical depth]. The evolution of the MTF for  $\text{Ly}\beta$  is plotted in Figure 3 (right panel). The error bars show the range of extremes of transmission within each bin, translated to optical depth.

We find that both the  $\text{Ly}\alpha$  and the  $\text{Ly}\beta$  MTFs are in excellent agreement<sup>3</sup> with observations at  $3 \lesssim z \lesssim 6$ . Though it might seem from Figure 3 that it is difficult to reach an optical depth as high as S04 at  $z = 6$  with our models, it must be noted that our results are weighed over a large number of realizations. In fact, we find that there are lot of realizations which give very high optical depth at  $z = 6$ , in complete agreement with S04.

Note that in the MTF analysis of the  $\text{Ly}\alpha$  forest, the slope of the equation of state  $\gamma - 1$  has been treated as a (non-evolving) free parameter which has the best-fit value  $\gamma = 1.3$ . Once that it is fixed in order to match the  $\text{Ly}\alpha$  data, no any other free parameter can be tuned to obtain a good trend of  $\text{Ly}\beta$  MTF. The agreement of the MTFs in both the  $\text{Ly}\alpha$  and  $\text{Ly}\beta$  regions is thus an indirect confirmation that the lognormal model for density fields could be considered as a fair description of the mildly non linear regime.

### 3.1.2 Probability Distribution Function (PDF)

In this Section, we compute the Probability Distribution Function of the transmitted flux for the  $\text{Ly}\alpha$  forest and compare it with the observed Keck spectra of SDSS 1044-0125, SDSS 1306+0356, and SDSS 1030+0524 within redshift range  $5.5 < z < 6.0$  (F02). In order to compare with observations, we add the relevant observational artifacts in our simulated spectra, i.e., we smooth the simulated spectra with a Gaussian filter of smoothing length  $\sigma_v = 28 \text{ km s}^{-1}$  (corresponding at a FWHM of  $66 \text{ km s}^{-1}$ ) and bin them

in pixels of width  $35 \text{ km s}^{-1}$ . We then add noise (see Section 2.1.5) to the simulated  $\text{Ly}\alpha$  forest spectra corresponding to the observed data with  $\sigma_{\text{noise}} = 0.02$ . Figure 4 shows the PDF of the transmitted flux, computed using 500 random realizations of the artificial spectra at the mean redshift 5.5, 5.7, 6.0 respectively.

The flux PDF of the simulated spectra is consistent with the observational ones in all three redshift cases. Furthermore, as expected, the agreement is quite good for both reionization models. Note that the difference in the photoionization rates of the two models are typically 18%, 18% and 39% for redshifts 5.5, 5.7, 6.0 respectively (see middle panel of Figure 1); yet the two models seem to be indistinguishable. This implies that the PDF is not sensitive enough in discriminating between different evolution histories of the ionizing background.

It is worth briefly mentioning here that F02 have used numerical simulations to compute the absorption spectra of high-redshift quasars in the  $\text{Ly}\alpha$  region and have found a rapid evolution of the volume-averaged neutral fraction of hydrogen at  $z \leq 6$  (from  $f_{\text{HI}} \sim 10^{-5}$  at  $z = 3$  to  $f_{\text{HI}} \sim 10^{-3}$  at  $z = 6$ ). This evolution has been interpreted as a signature of the end of reionization around  $z \approx 6$ . However, we find that, in addition to late reionization models (where  $f_{\text{HI}}$  is evolving rapidly at  $z \approx 6$ ), early reionization models also give a good fit to the observed MTF and PDF at  $z \leq 6$ . It is thus *not* possible to rule out early reionization models using only MTF and PDF statistics at  $z \lesssim 6$ .

### 3.1.3 Dark Gap Width Distribution (DGWD)

At high redshifts, regions with high transmission in the  $\text{Ly}\alpha$  forest become rare. Therefore an alternative method to analyze the statistical properties of the transmitted flux is the distribution of dark gaps first suggested by Croft (1998), defined as contiguous regions of the spectrum having an optical depth  $>$  than 2.5 over rest frame wavelength intervals greater than  $1 \text{ \AA}$ . In this Section we will com-

<sup>3</sup> The fact that there is hardly any difference between the early and late reionization models is related to the fact that the two models differ substantially only at redshifts above 6.

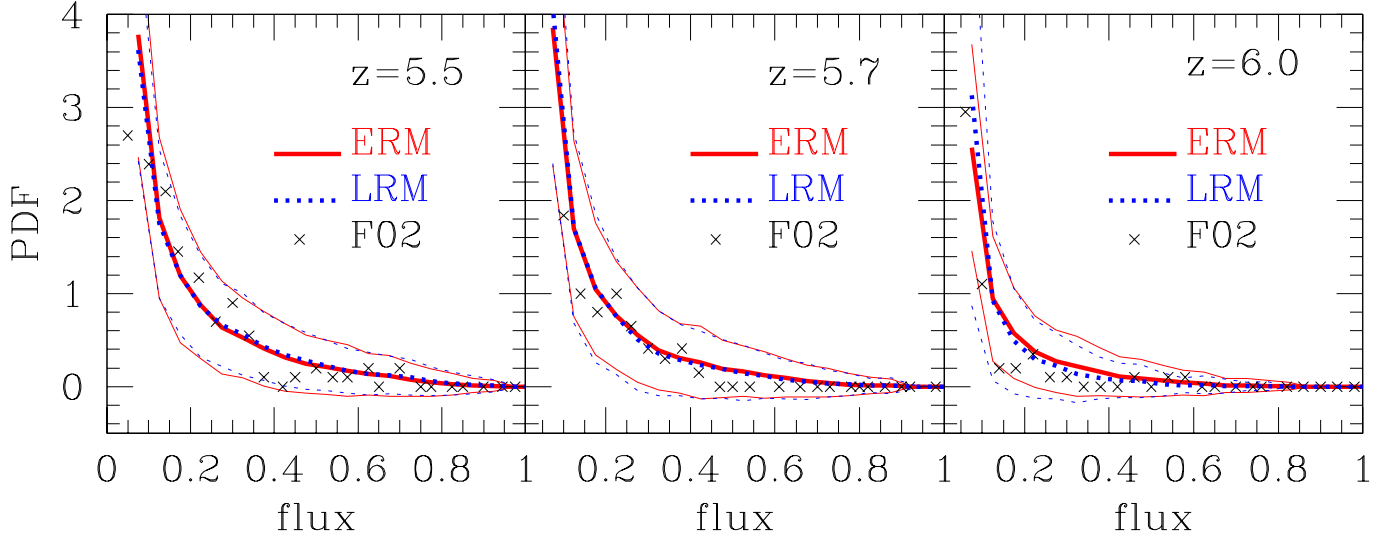


**Figure 4.** Probability distribution function of the transmitted flux at mean redshift 5.5, 5.7 and 6.0, respectively, compared with F02 Keck data. Solid (red) and dotted (blue) lines represent the ERM and the LRM, respectively. For each model, the thick line is the average over 500 LOS, the thin lines denote the cosmic variance.

pare our results with observational data obtained by Songaila & Cowie (2002), hereafter SC02, analyzing 15 high-redshift QSOs whose emission redshifts lie in  $4.42 \lesssim z \lesssim 5.75$ . In order to obtain a fair comparison with data, each simulated spectrum has been convolved with a Gaussian having FWHM equal to  $60 \text{ km s}^{-1}$ , resulting in a spatial resolution similar to the data obtained using ESI spectrograph. In Figure 5 we plot typical simulated line of sight spectra at redshifts 4.61 and 5.74. The black lines plotted immediately below the spectra show the regions identified as gaps in the  $\text{Ly}\alpha$  region and the ones below those show the gaps present in the  $\text{Ly}\beta$  region too. This Figure should be compared with Fig 2 of SC02, showing good qualitative agreement between our results and observations. It is also clear from the Figure that the frequency and the width of the gaps increase from redshift 4.61 to redshift 5.74.

Figure 6 shows the DGWD for the redshift range  $3.0 < z_{\text{abs}} < 5.5$  (where  $z_{\text{abs}}$  is the redshift of the absorber), obtained from a sample of 300 LOS for each redshift bin. The distribution essentially measures the number of gaps having a certain width  $W_\alpha$  in the QSO rest frame within the  $\text{Ly}\alpha$  region. The results, as well as the statistical errors, obtained from our models are in good agreement with observational data over a wide redshift range. One can also see that the frequency of larger gaps increases as we go to higher redshifts. Comparing our results with hydrodynamical simulations (Paschos & Norman 2005) we find that our results are in better agreement with observations. This is probably due to their limited box size ( $6.8 \text{ comoving } h^{-1} \text{ Mpc}$ ); in this case to simulate spectra covering a large redshift range (5.0–5.5, for instance) each line of sight has to cross the simulated volume more than once. So the presence of an under-ionized region could break a long dark gap in smaller ones. The advantages of using semi-analytical simulation is that we can obtain the same length of the observed spectrum (e.g.  $100 \text{ \AA}$  to compare with SC02) in one realization, instead of combining together various artificial spectra end to end.

So far we have tested our models against the observational data available at  $z < 6$ . We have seen that both late and early reionization models are able to match (i) the MTF evolution both in the  $\text{Ly}\alpha$  or  $\text{Ly}\beta$  regions, (ii) the PDF of the transmitted flux and finally

(iii) the DGWD. We can thus conclude that the results obtained at  $z < 6$  do not allow to exclude the possibility that the universe has been reionized as early as at redshift 14. However, we have already discussed the fact that the difference between the two reionization scenarios are most substantial only at  $z > 6$ . It is thus important to see how the  $\text{Ly}\alpha$  forest at  $z > 6$  can be used for distinguishing between the two different scenarios. This is what will be done in the next Section.

### 3.2 Predictions for higher redshifts

Let us now extend the analyses of the previous Section to spectra at  $z > 6$  and try to determine whether the  $\text{Ly}\alpha$  forest is able to distinguish between different models of reionization. Since the spectra are generally expected to be much darker at these high redshifts, it is clear that the MTF would not be able to distinguish between the two models (it is consistent with zero irrespective of the ionization state of the IGM). Hence, we start our discussion with the PDF of the transmitted flux for the  $\text{Ly}\alpha$  forest.

#### 3.2.1 Probability distribution function (PDF)

As in the Section 3.1.2, we compute the PDF of the transmitted flux for 500 random LOS, with the corresponding cosmic variance. The results are shown in Figure 7 for mean redshifts of 6.25 and 6.5, respectively. Interestingly, we find that even at redshifts higher than 6 (where the ERM and LRM differ quite substantially in their physical properties), the PDF is not able to differentiate between the two reionization scenarios mainly because of large cosmic variance. This has to do with the fact that most of the pixels have flux consistent with zero for both reionization models and so the PDF essentially probes the noise distribution (which is independent of the physical state of the IGM). However, note that in the LRM we have *no* pixels with  $F > 0.8$  at  $z = 6.25$  and with  $F > 0.7$  at  $z = 6.5$  respectively, while there are pixels (though very few) with  $F$  as high as 0.85 at  $z = 6.25$  and 0.8 at  $z = 6.5$  for the ERM (these correspond to some peaks present in the ERM which are suppressed in the LRM). Whether this can discriminate between

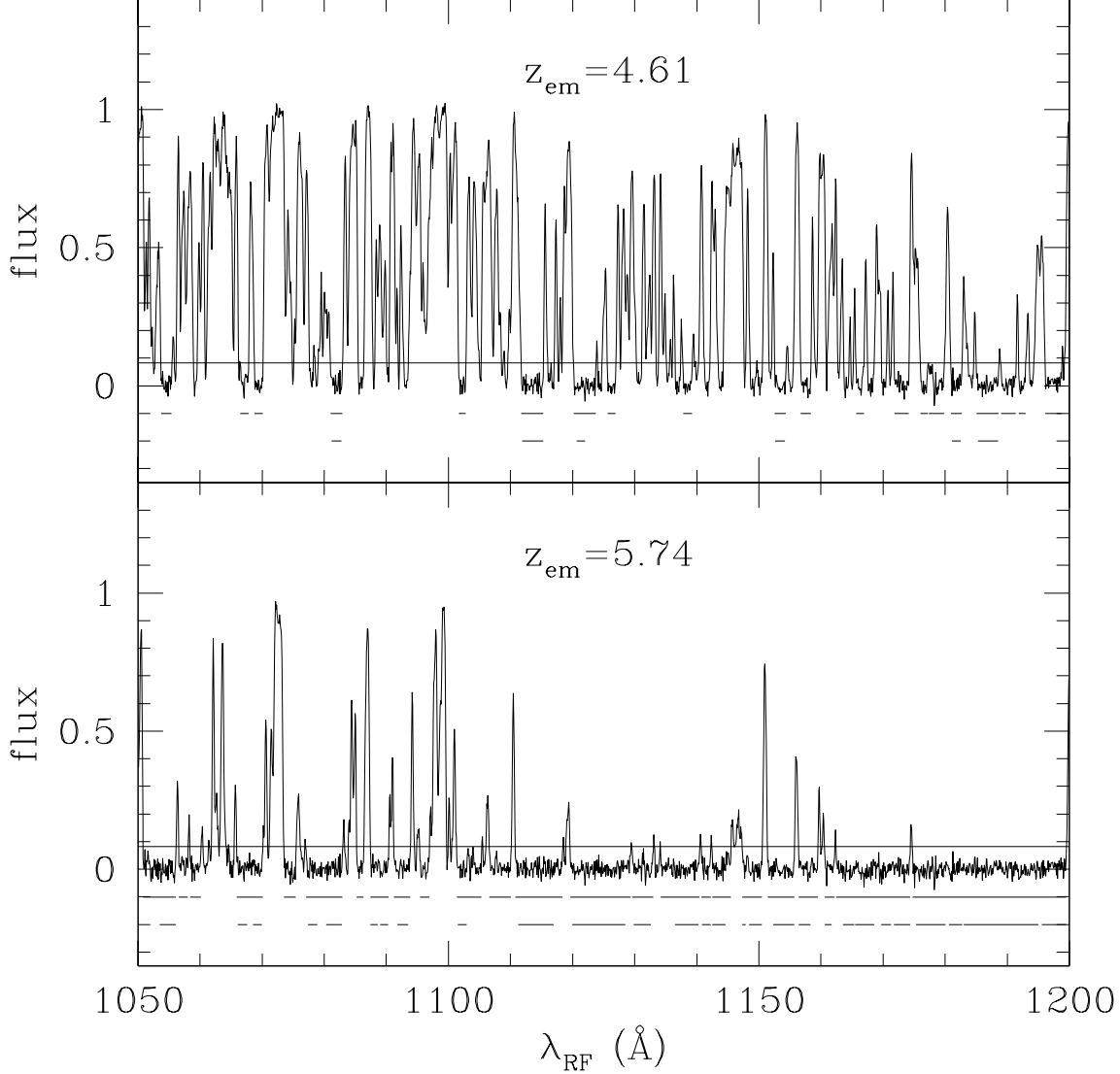


**Figure 5.** Two simulated QSO spectra with emission redshift 4.61 (top panel) and 5.74 (bottom panel). The broken lines immediately below the spectra represents dark gaps in the  $\text{Ly}\alpha$  region and the ones below those show the analogous gaps in the  $\text{Ly}\beta$  region. The horizontal solid lines slightly above zero transmission represent the flux threshold ( $= 0.082$ ) used for defining gaps.

the two models is doubtful particularly because of the uncertainties in the continuum of the unabsorbed quasar spectra and the effects arising from atmospheric absorption.

### 3.2.2 Dark Gap Width Distribution (DGWD) at $z > 5.5$

The next statistics which can be used is the DGWD for the  $\text{Ly}\alpha$  forest at redshifts higher than 5.5. For definiteness, we consider two redshift intervals: 5.7 – 6.3 and 6.0 – 6.6. The first case should be applicable to QSOs having emission redshift around 6.4, while the second case corresponds to an emission redshift  $\approx 6.7$ . In Figure 8, we plot sample spectra for the two different reionization models in the redshift range 5.7 – 6.3, with the upper (lower) panel corresponding to ERM (LRM). The black lines plotted immediately below the spectra show the regions identified as gaps. Note that

the two spectra have the same baryonic density distribution and differ only in the distribution of neutral regions. It is clear that at large values of rest frame wavelengths ( $\lambda_{\text{RF}}$ ), say,  $\lambda_{\text{RF}} > 1150$  Å (which corresponds to  $z > 6$ ), there are substantial differences between the ERM and LRM. The LRM does not have the peaks at large redshifts which are present in the ERM, and hence one obtains gaps of much larger widths for the LRM. The reason for the suppression of the peaks in the LRM is twofold. Firstly there is an increase in the optical depth at the pixels where neutral regions are placed, thus decreasing the transmission. However, there is a second effect which seems to be more important which has to do with the damping profile of neutral hydrogen arising from natural line width. This effect can suppress flux in regions which are not necessarily neutral but lie in the vicinity of a highly neutral region. This can be understood from a close-up of the spectra shown

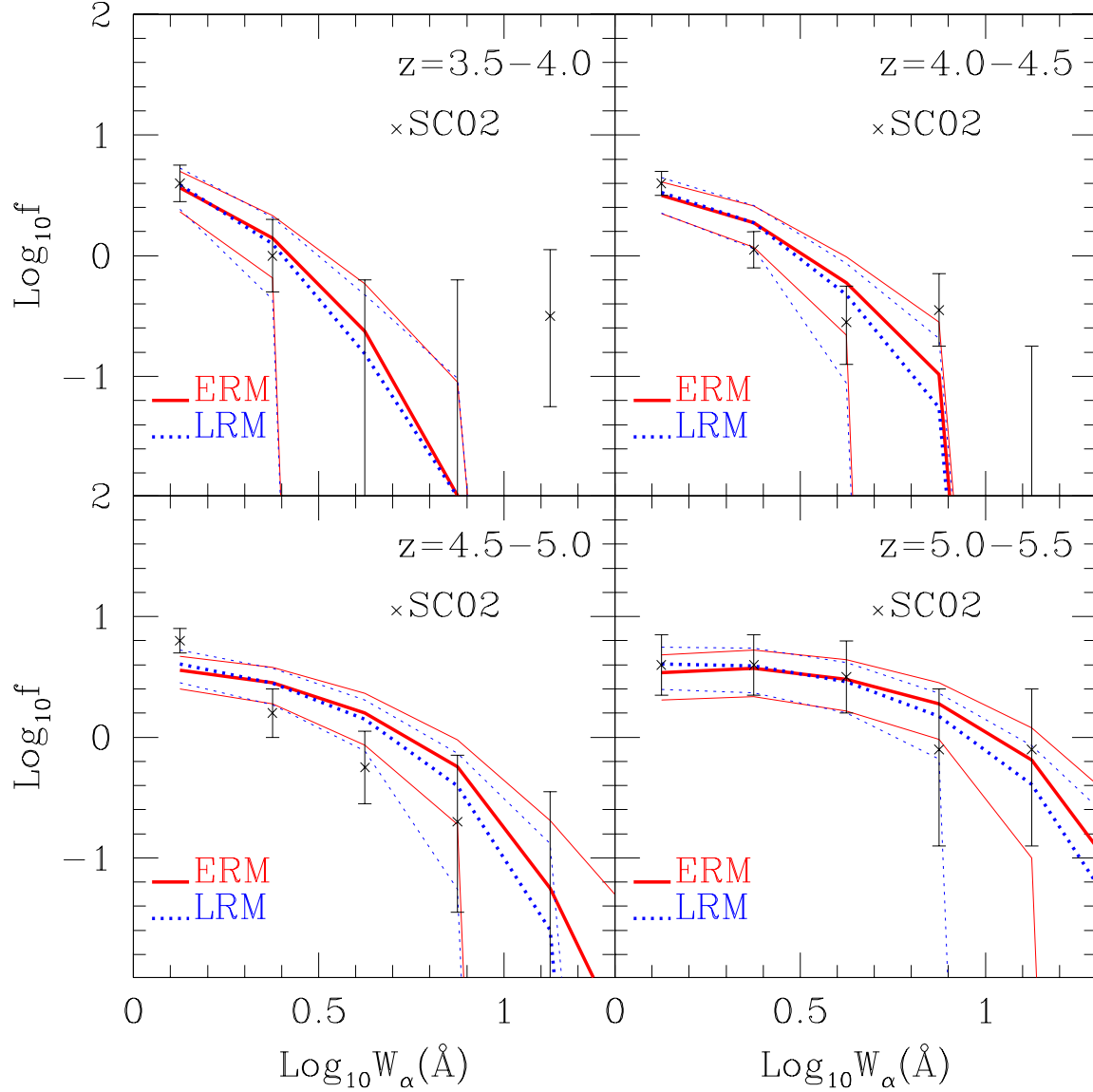


**Figure 6.** Dark Gap Width Distribution (DGWD) at redshift 3.5–5.5 compared with Songaila & Cowie (2002), denoted SC02 in the panels. Solid (red) and dotted (blue) lines represent the ERM and the LRM, respectively. For each model, the thick line is the average over 300 LOS, the thin lines denote cosmic variance.

in Figure 9 where we have zoomed into a region between  $1191 \text{ \AA} < \lambda_{\text{RF}} < 1194 \text{ \AA}$ . As before the upper (lower) panel corresponds to ERM (LRM) and the black lines plotted immediately below the spectra show the regions identified as gaps. We have also shown the positions of the neutral pixels by crosses within the Figure. Note that there are two prominent peaks in the ERM at  $\lambda_{\text{RF}} = 1192.2 \text{ \AA}$  and  $1193.4 \text{ \AA}$  respectively while they are completely suppressed in the LRM. However, note that there are *no* neutral pixels at the location of the peaks – they are actually suppressed by the damping wings of a small number of neutral pixels in the vicinity. Thus the damping wing of neutral regions can have a dramatic effect on the distribution of dark gap widths as shall be discussed next.

The results for the distribution of dark gap widths for the two redshift ranges are plotted in Figure 10. We find that the dark gap width distributions for ERM and LRM are essentially the same (ac-

counting for the cosmic variance) for  $W_\alpha < 40 \text{ \AA}$ , where  $W_\alpha$  denotes the gap width in the Ly $\alpha$  forest. However, one should note that for larger  $W_\alpha$  the frequency of gaps differs substantially for different models, with the difference being quite obvious for the redshift range  $6.0 - 6.6$ . As expected, LRM predicts an higher probability to find larger gaps because of the neutral regions in the IGM. This difference in the two models at large gap widths can be used as a possible discriminator between early and late reionization. However, it turns out that it is possible to devise a more sensitive statistics for this purpose which we discuss in the next subsection.

### 3.3 Distribution of largest gaps

In this Section, we present the most sensitive diagnostic for distinguishing between different reionization scenarios using the Ly $\alpha$

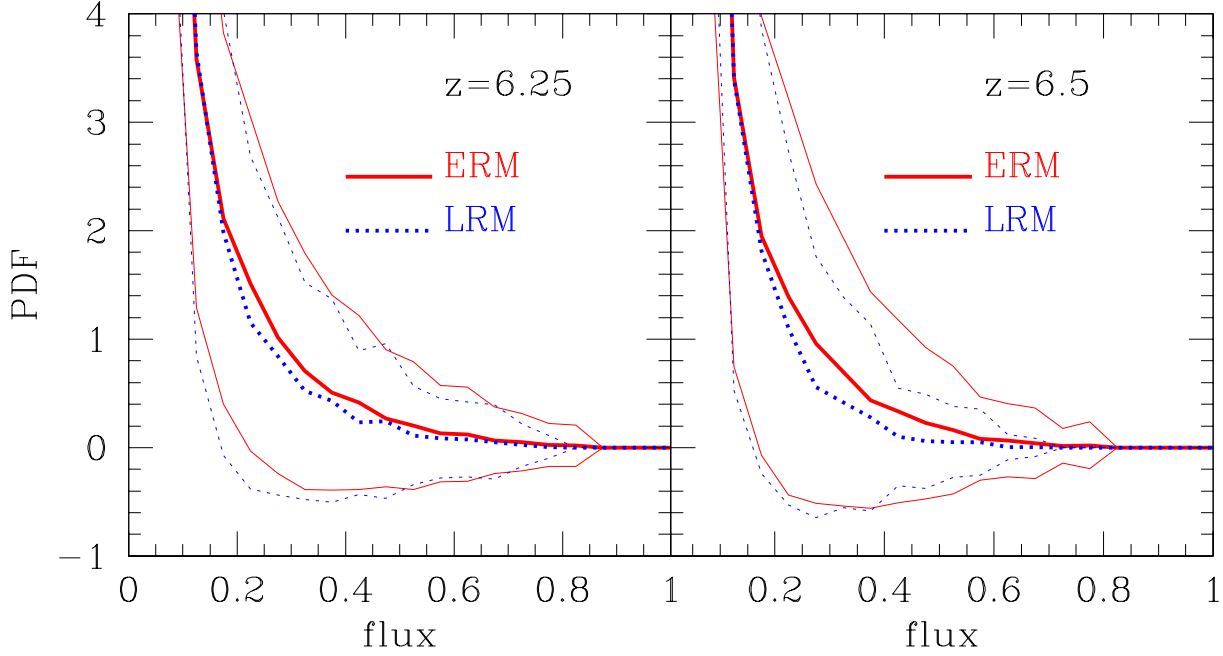


Figure 7. Same as in Figure 4 but at mean redshifts 6.25 and 6.5.

forest. We calculate the width of the largest gap  $W_{\alpha}^{\max}$  for each of the 300 LOS generated from our models, and then compute the fraction of LOS having a particular value of the largest gap width. It is clear from the discussion on Figure 8 that the typical size of the largest gap along a LOS will be much larger in the LRM compared to ERM. The fraction of LOS having a given value of largest gap is shown in Figure 11 with the corresponding cosmic variance. It is clear that the distributions for the two models differ substantially; in particular, one should find gaps with  $W_{\alpha} > 50 \text{ \AA}$  for the LRM along  $\sim 35$  per cent of the lines of sight, while if the universe is ionized early, there should be *no* line of sight with a dark gap width  $> 50 \text{ \AA}$ . This is a very stringent result, and can be used to rule out the early reionization scenario from observational data. Similarly, the absence of dark gap widths  $> 50 \text{ \AA}$  can be used to rule out late reionization scenarios.

As expected, the difference between the two reionization models is more drastic in the highest redshift range 6.0 – 6.6. In particular, we expect nearly half the lines of sight to have a gap of width as large as  $80 \text{ \AA}$  if the universe is in the pre-overlap stage, while no such line of sight should be observed if the IGM is ionized. Even if we take the statistical errors into account, we find that in order to validate the late reionization hypothesis, at least 40 per cent of the lines of sight should have dark gaps larger than  $70 \text{ \AA}$  in the redshift range 6.0 – 6.6.

At present SDSS has already observed 9 QSOs above redshift 6, and thus one should be able to compute the distribution of the largest gap widths. As an example, a visual inspection of the spectra of QSO SDSS J1030+0524 (which shows the darkest GP trough till date) reveals that the size of the largest dark gap is  $< 40 \text{ \AA}$ , which can be well explained both by ERM and LRM.

### 3.4 Peak Width Distribution (PWD)

Having identified a very useful statistics, the DGWD, we now introduce another possible analysis which can be thought as complementary to the gap statistics. The Peak Width Distribution (PWD)

allows us to measure the frequency and the width of those regions of the spectra characterized by a high transmission, i.e., a flux between 0.08 and 0.8 over rest frame wavelength intervals greater than  $0.2 \text{ \AA}$  (which is roughly equal to 6 pixels of our rebinned spectra). Visually these regions would appear as isolated spikes in the spectra at high redshifts (in this sense the terms “spike” and “gap” can be thought of as equivalent). The lower threshold flux is same as the one used as the upper threshold in the DGWD analysis, while the upper limit value of 0.8 have been chosen in order to avoid regions of full transmission which could be affected by atmospheric absorption (though this effect does not seem to have much effect on the statistics). Figure 12 shows the results for the PWD in the redshift ranges 5.7 – 6.3 and 6.0 – 6.6, respectively with  $P_{\alpha}$  denoting the width of the peak. Similar to the DGWD, it is clear that for small peak widths, the errors are too large and thus do not allow to use this statistics for discriminating between the two models; however the distributions are quite different for peak widths larger than  $1.2 \text{ \AA}$ . This suggests that the fraction of lines of sight having a largest peak width of a given value could be used as another discriminating statistics between the two models.

The results for the fraction of lines of sight with a given value of the largest peak width  $P_{\alpha}^{\max}$  are plotted in Figure 13. It seems that at  $z = 5.7\text{--}6.3$ , the probability of finding a line of sight having a peak width larger than  $1.2 \text{ \AA}$  is negligible in the LRM, while in an ERM peaks of this size seem to be present for 20 per cent of the lines of sight. The same effect is more evident in the redshift range 6.0 – 6.6: there ERM predicts peaks of width  $\sim 1 \text{ \AA}$  in 40 per cent of the lines of sight; on the contrary, the LRM predicts no peaks larger than  $0.8 \text{ \AA}$ .

We believe that the distribution of peak widths can be used in a complementary way with the dark gap width statistics for constraining the ionization state of the IGM at  $z \gtrsim 6$ .

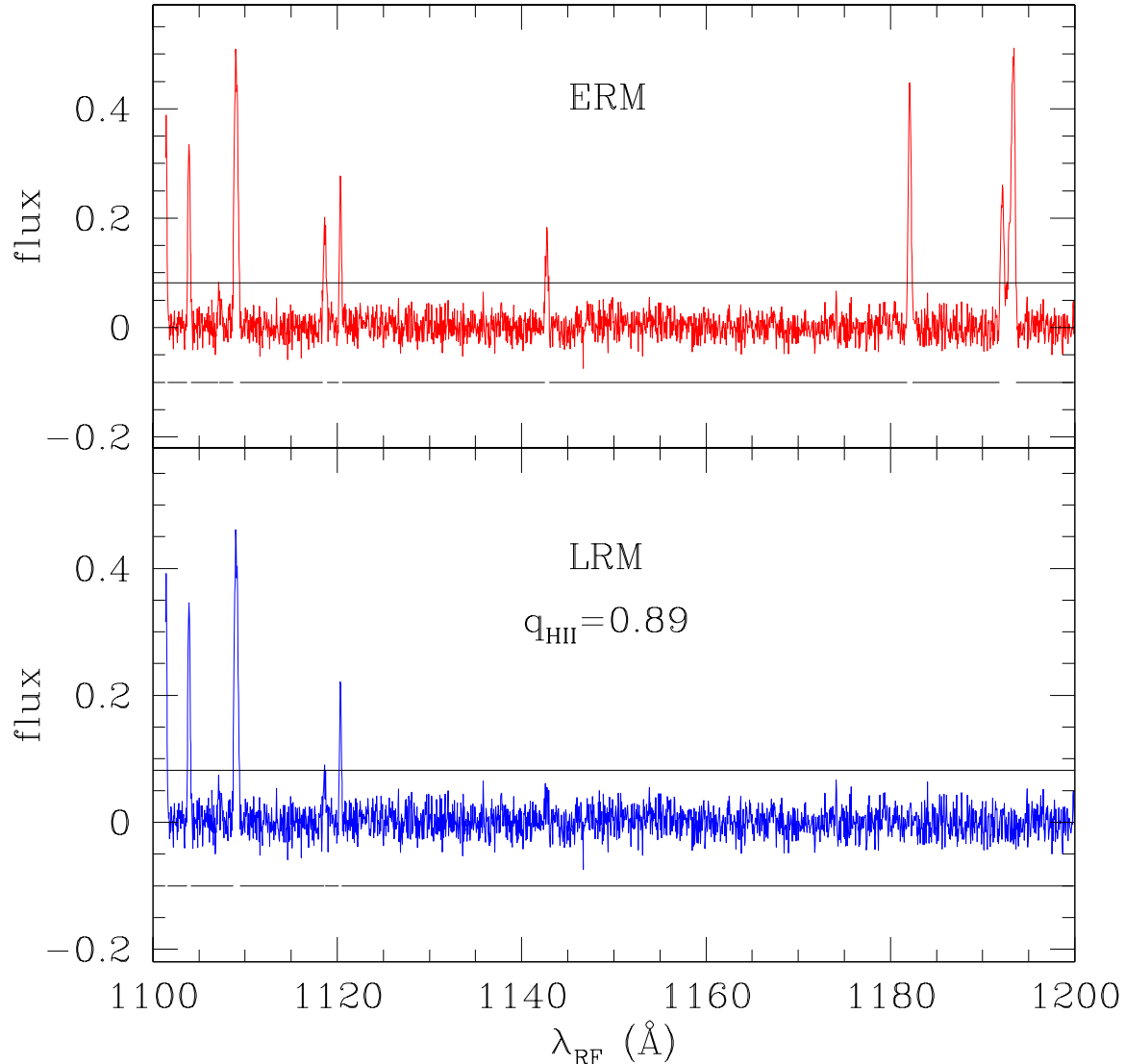


**Figure 8.** Comparison between two simulated spectra for different reionization scenarios, ERM (top panel) and LRM (bottom panel), in the redshift range 5.7–6.3. Both these spectra are obtained from the same density distribution.

### 3.5 Results for the $\text{Ly}\beta$ region

In addition to the  $\text{Ly}\alpha$  forest, one can also use the  $\text{Ly}\beta$  region of the absorption spectra to constrain the ionization state of the IGM at high redshifts. The advantage of using the  $\text{Ly}\beta$  absorption lines is that the absorption cross section is lower than the  $\text{Ly}\alpha$  one, and hence one finds some features of transmission within the spectra in  $\text{Ly}\beta$  region even when  $\text{Ly}\alpha$  transmission is zero. In this Section, we present our predictions for the  $\text{Ly}\beta$  forest at  $z > 6$ .

We have calculated the DGWD for the  $\text{Ly}\beta$  forest in the redshift ranges of interest and found it to be quite similar to the  $\text{Ly}\alpha$  case. The distribution does show some differences between the reionization models at high values of gap widths, though the difference is not as evident as in the case of  $\text{Ly}\alpha$ . We plot the fraction of LOS having a largest gap width of a given value in Figure 14, which corresponds to Figure 11 for  $\text{Ly}\alpha$ . Though the ERM and the

LRM differ in their distributions for  $\text{Ly}\beta$  regions, we find that it is not as discriminating as in the case of  $\text{Ly}\alpha$  in the redshift intervals considered here.

We have also computed the PWD distribution for the  $\text{Ly}\beta$  region of the spectra. The broad conclusions are similar to those obtained from  $\text{Ly}\alpha$  regions, though the discrimination between LRM and ERM is reduced in the case of  $\text{Ly}\beta$ . However, the usefulness of  $\text{Ly}\beta$  statistics lies in the fact that these can be used as an independent check for the reionization models.

### 3.6 Dark gaps in both $\text{Ly}\alpha$ and $\text{Ly}\beta$ regions

In this Section we study the presence of dark gaps in both the  $\text{Ly}\alpha$  and the  $\text{Ly}\beta$  regions of the absorption spectra. In Figure 15 we show the mean  $\text{Ly}\alpha$  against the mean  $\text{Ly}\beta$  optical depth for different dark gap lengths, for both reionization

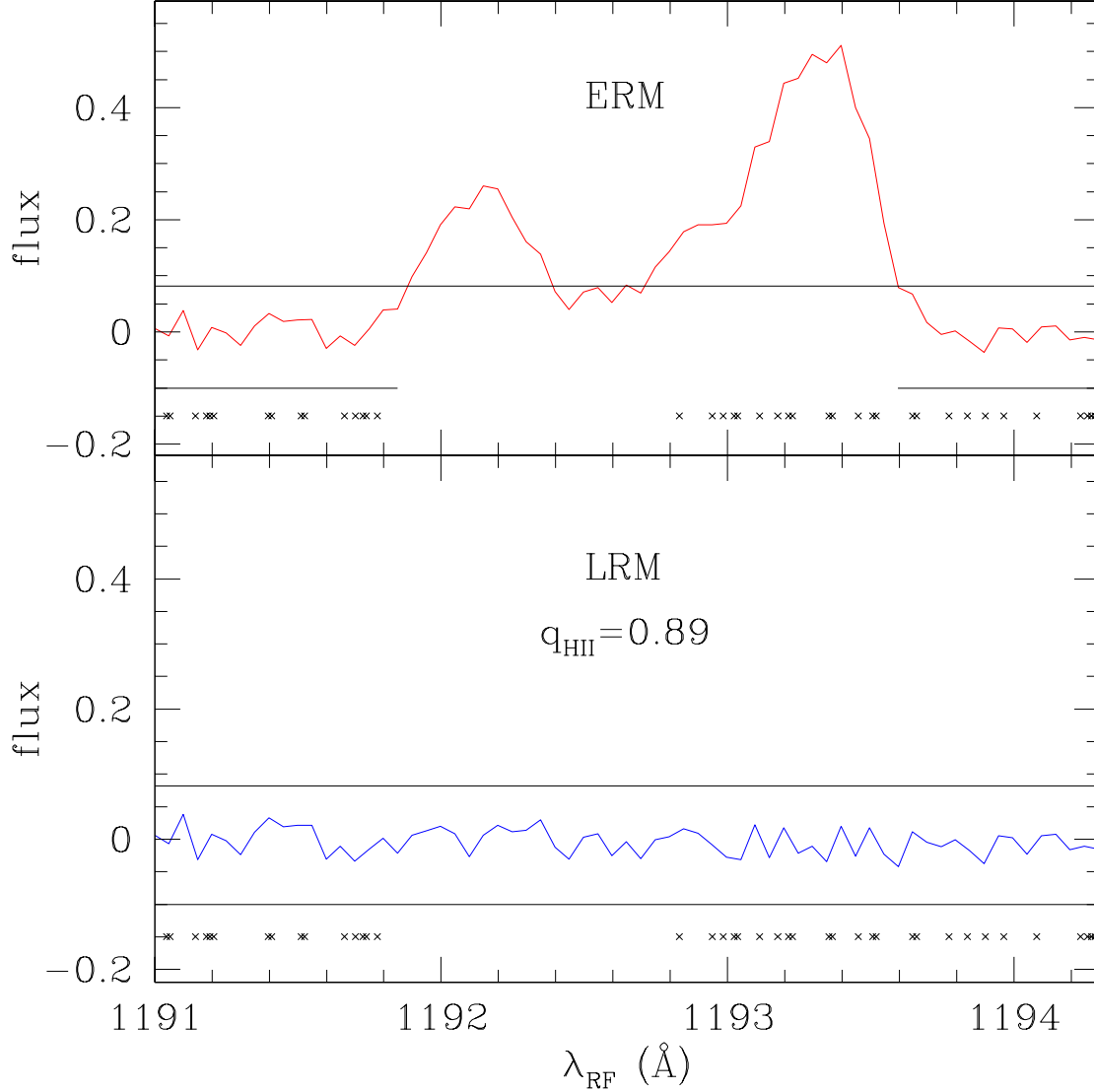


**Figure 9.** Same as in Figure 8, but zoomed into the spectral region  $1191 \text{ \AA} < \lambda_{\text{RF}} < 1194 \text{ \AA}$ . The black lines plotted immediately below the spectra show the regions identified as gaps. We have also shown the positions of the neutral pixels by crosses. Even if neutral pixels are present only in the LRM, we draw them also in the ERM spectrum, in order to visualize their location. It is evident that there is suppression of the flux in the LRM even if there are no corresponding neutral pixels. This result, as discussed in detail in the text, is due to the damping wings of the neighboring neutral pixels.

models. Points and triangles in the figure represent dark gaps such that  $0 \leq \log_{10}[\text{Max}\{W_\alpha, W_\beta\}] \leq 0.5$  and  $1.5 \leq \log_{10}[\text{Max}\{W_\alpha, W_\beta\}] \leq 2$ , respectively, where  $\text{Max}\{W_\alpha, W_\beta\}$  is the width of the larger dark gap between the  $\text{Ly}\alpha$  and  $\text{Ly}\beta$ . It is obvious from the figure (and also stressed by Paschos & Norman 2005) that larger dark gaps correspond to higher optical depths in both models.

There is one more interesting point to be noted from the figure. Conventionally the total  $\text{Ly}\beta$  optical depth is obtained from the  $\text{Ly}\alpha$  one, using the following relation:

$$\tau_{\text{Ly}\beta}^{\text{tot}}(z) = 0.16\tau_{\text{Ly}\alpha}(z) + \tau_{\text{Ly}\alpha}(z_\beta), \quad (26)$$

which assumes that  $\tau_{\text{Ly}\beta}(z) = 0.16\tau_{\text{Ly}\alpha}(z)$ . This assumption is true for low column density systems when the line profile of ab-

sorption is determined by the velocity field and is same for  $\text{Ly}\alpha$  and  $\text{Ly}\beta$ . In this case, the points in the  $\tau_{\text{Ly}\beta}^{\text{tot}} - \tau_{\text{Ly}\alpha}$  plane will be strictly bound by a lower envelope, which will correspond to a straight line having a slope of 0.16. This bound is shown in the figure as the slanted solid line. Note that for ERM there are truly no points below this line. On the other hand, for LRM there are a lot of points below the solid line with slope 0.16. This is related to the fact that the absorption from neutral regions present in the LRM cannot be described by a simple Gaussian profile and one has to take into account the effect of damping wings. This means that, as already discussed in Section 2.1.4, the usual adopted way to compute the total  $\text{Ly}\beta$  optical depth from the  $\text{Ly}\alpha$  one using equation (26) it is not appropriate in general, particularly when the neutral

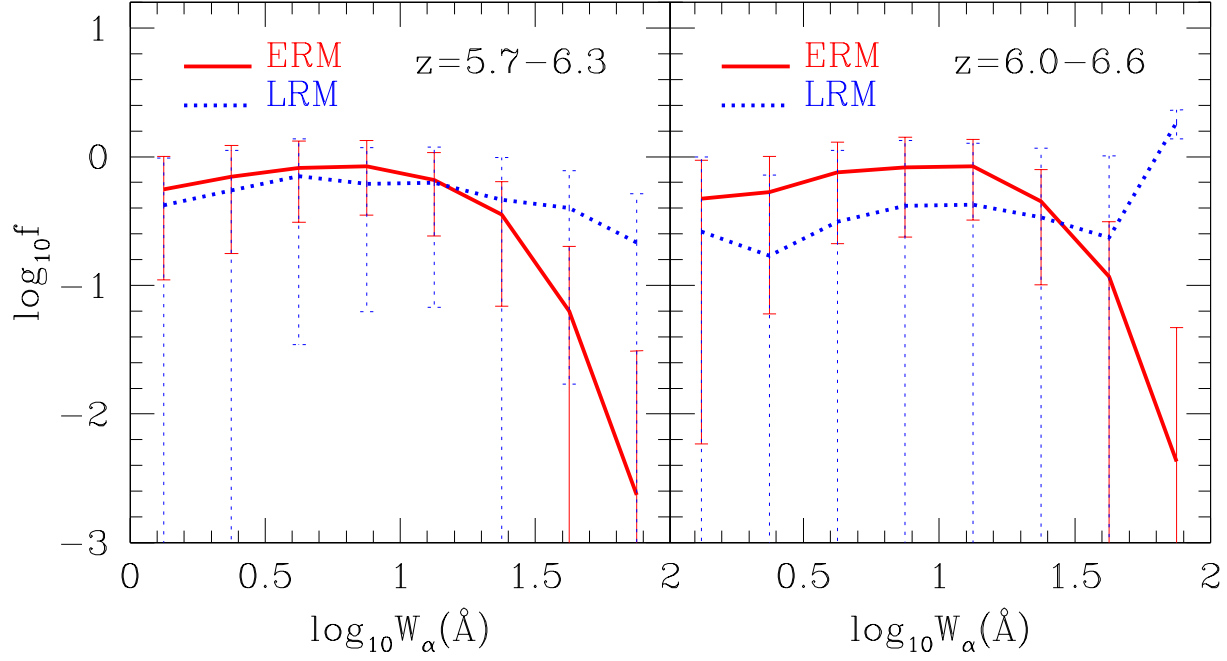


**Figure 10.** Dark Gap Width Distribution (DGWD) at redshift 5.7–6.3 (left) and 6.0–6.6 (right). Solid (red) and dotted (blue) lines represent the ERM and the LRM, respectively. For each model, the thick line is the average over 300 LOS, the error bars denote cosmic variance.

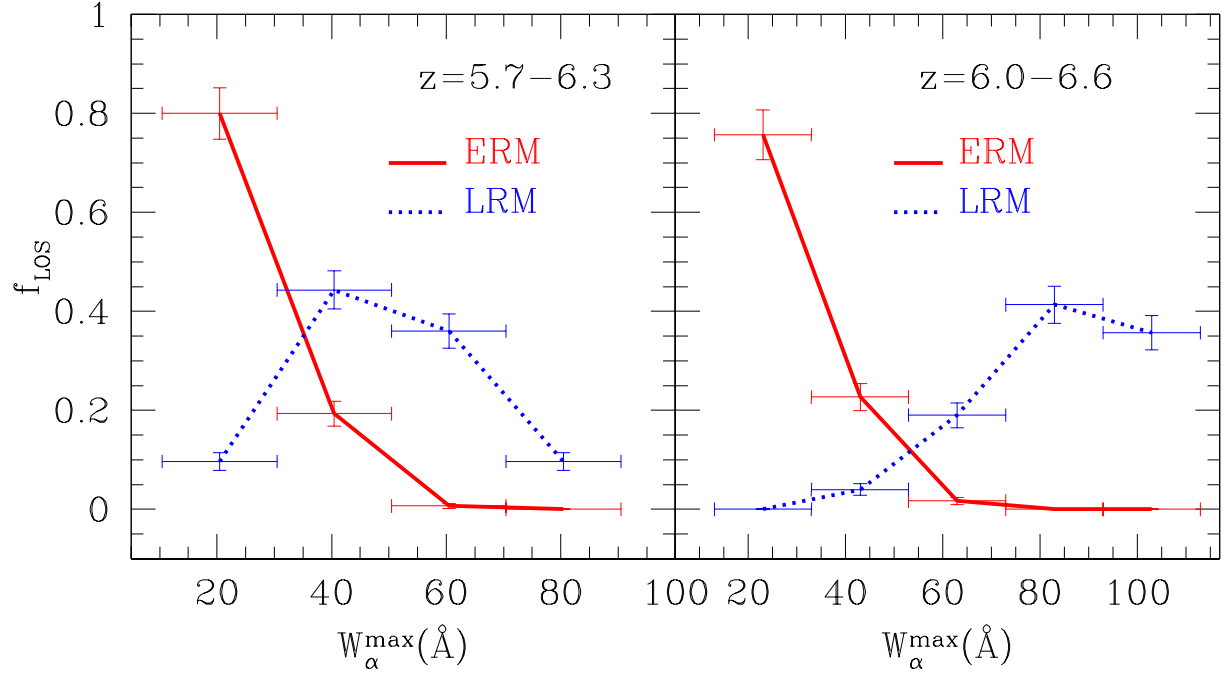


**Figure 11.** Distribution of the largest dark gap widths  $W_{\alpha}^{\max}$  for 300 LOS in the redshift range 5.7–6.3 (left panel) and 6.0–6.6 (right panel) for ERM (solid red line) and LRM (dotted blue line). The vertical error bars denote the cosmic variance; the horizontal error bars show the bin size.

fraction of the gas is high and the Lorentzian part of the line profile becomes important.

### 3.7 Variations in the Late Reionization Models

We now discuss certain other possibilities regarding the distribution of neutral regions along lines of sight. So far we have been using LRM as the fiducial model for late reionization which as-

sumes that the neutral regions are distributed randomly, and they have *no* correlation with the density field. However, this is not the only possible way to distribute the neutral pixels. Hence we study two variations of the LRM which are named LRMD (d=density) and LRMC (c=clustered). The LRMD is similar to LRM except that within a given redshift range the neutral pixels are correlated with the density field with high density regions being preferentially neutral. In the case of LRMC, we assume that the neutral regions are

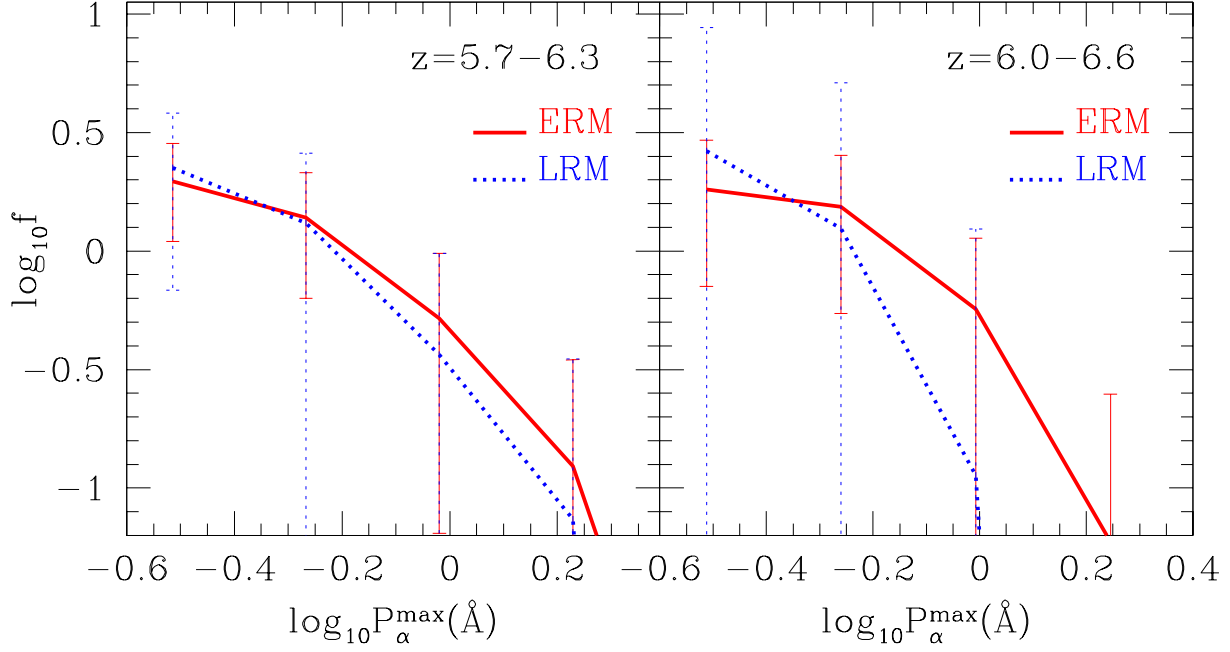


**Figure 12.** PWD at redshift ranges 5.7–6.3 (left panel) and 6.0–6.6 (right panel). Solid (red) and dotted (blue) lines represent the ERM and the LRM, respectively. For each model, the thick line is the average over 300 LOS, the error bars denote cosmic variance.

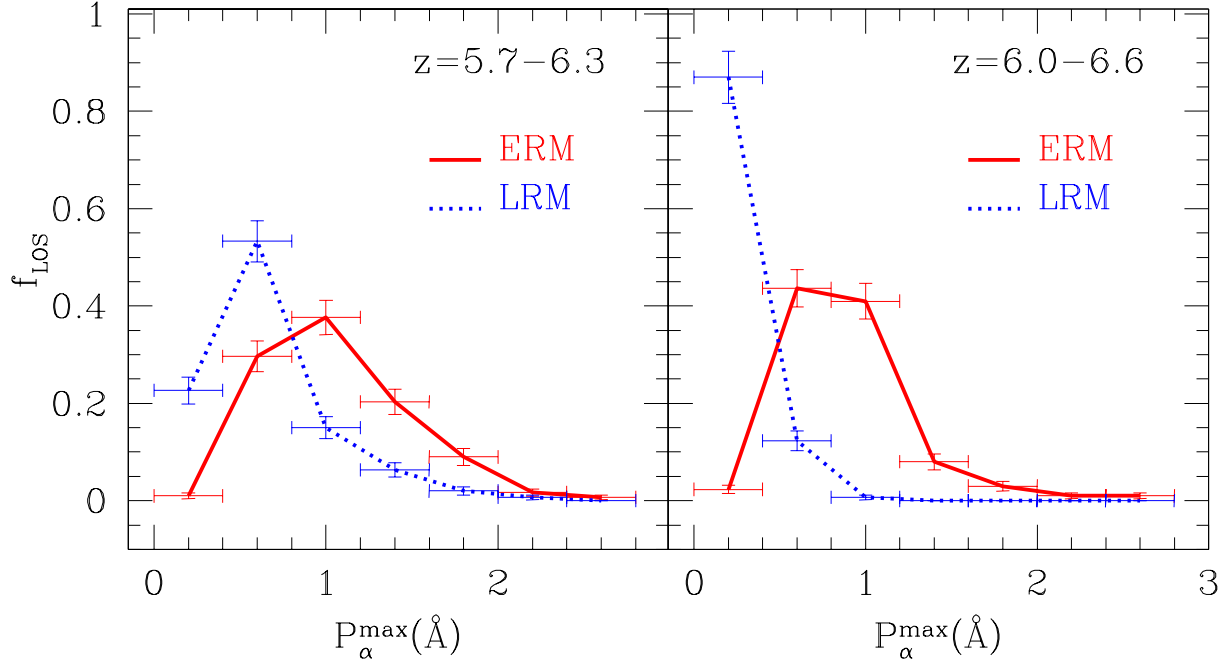


**Figure 13.** Same as in Figure 11 but for largest peak widths  $P_{\alpha}^{\max}$ .

maximally clustered (i.e., they form a large coherent structure along the line of sight) when calculating the one-dimensional filling factor,  $q_{\text{HII}}$ . This assumption represents the most extreme alternative to the LRM. In constructing our models we do not expect to recover exactly the real distribution of neutral regions; however, as we are considering the most extreme cases we expect the actual distribution to be somewhere between the two. In the LRMc we find that the IGM is characterized by highly clustered large neutral regions (of lengths as large as few tens of comoving Mpc) and the correla-

tion of these regions with the density field does *not* have any effect on the simulated spectra. The technical details on how we generate these models are discussed in Appendix B.

We start with the qualitative description of sample spectra for the three models as shown in Figure 16. We recall that all the three panels have the same baryonic distribution and same value of  $q_{\text{HII}}$  along the line of sight (i.e., the number of neutral pixels, denoted by crosses, in the three panels are equal although it may not be visually obvious).

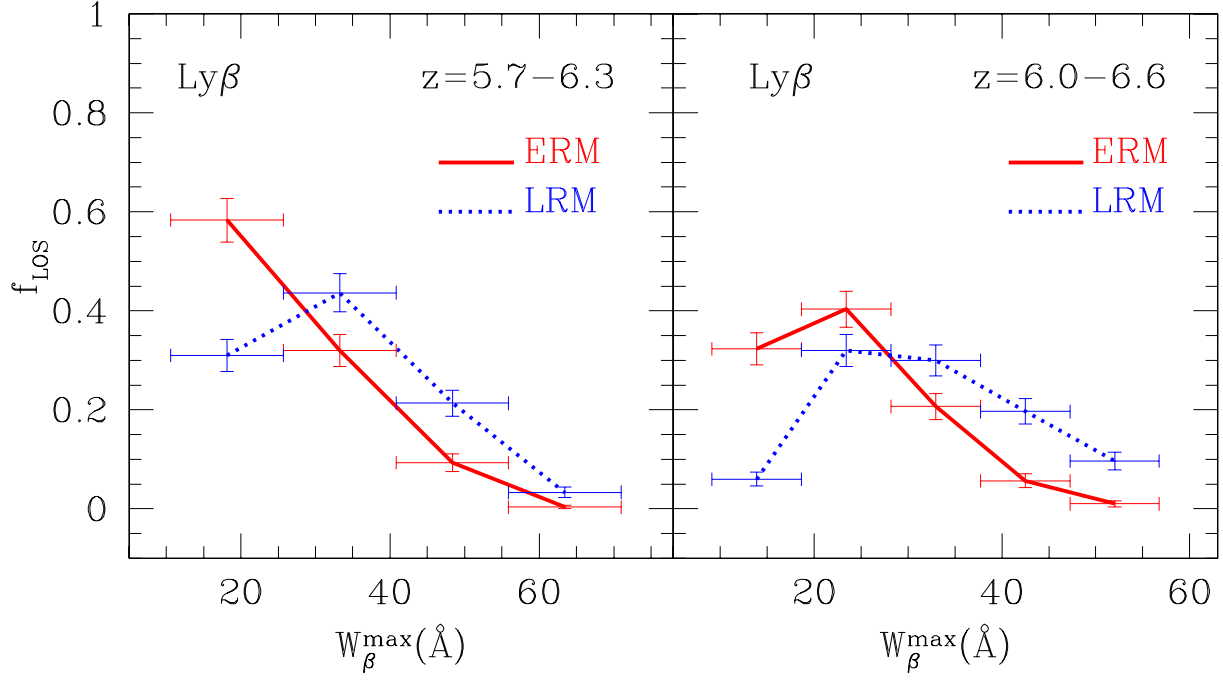
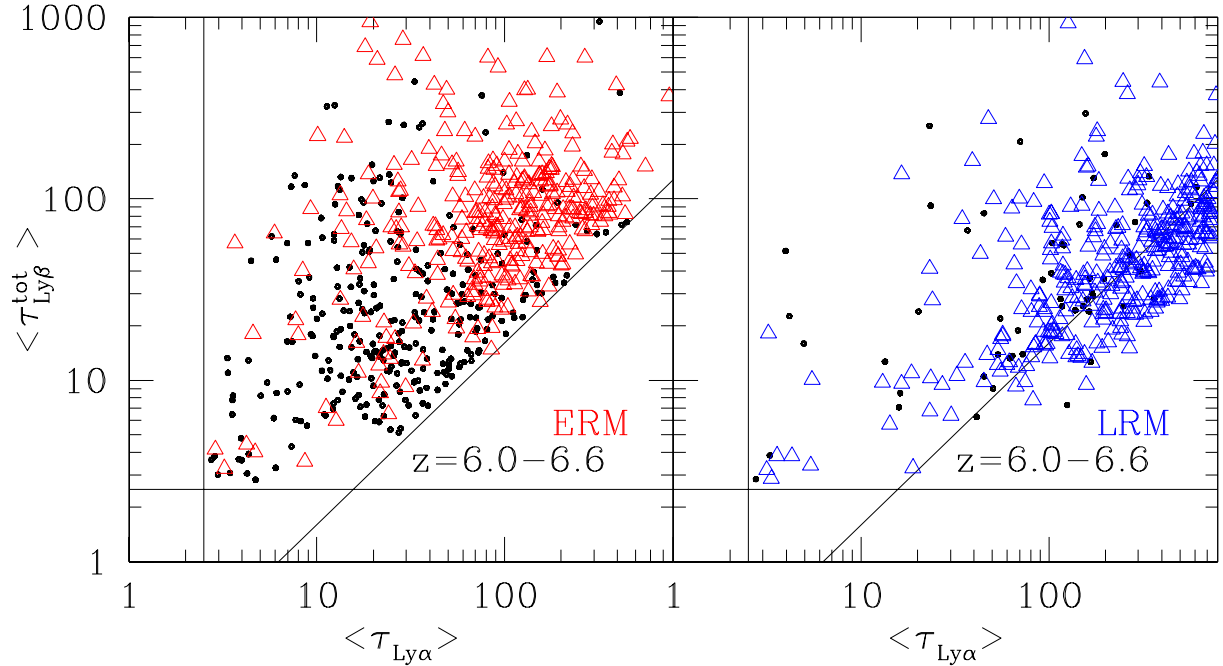


Figure 14. Same as in Figure 11 but for the Ly $\beta$  region.



**Figure 15.** Scatter plot of the mean Ly $\alpha$  and the mean Ly $\beta$  optical depths for each dark gap. Points and triangles represent dark gap such that  $0 \leq \log_{10}[\text{Max}\{W_\alpha, W_\beta\}] \leq 0.5$  and  $1.5 \leq \log_{10}[\text{Max}\{W_\alpha, W_\beta\}] \leq 2$ , respectively, where  $\text{Max}\{W_\alpha, W_\beta\}$  is the width of the largest between the Ly $\alpha$  and Ly $\beta$  dark gaps. The solid lines parallel to the axes represent Ly $\alpha$  and Ly $\beta$  optical depths equal to 2.5, which acts as the lower limit for defining gaps. The slope of the slanted solid line is equal to the ratio  $(f_{\text{Ly}\beta} \lambda_{\text{Ly}\beta}) / (f_{\text{Ly}\alpha} \lambda_{\text{Ly}\alpha}) = 0.16$ .

The first point to note is the similarity between the LRM and LRMd, implying that the correlation of the neutral segments with the density field does not have much of an effect on the Ly $\alpha$  forest. Although there are small differences in the actual positions of the neutral pixels in the two models, the gap widths are exactly similar for this line of sight. There are differences in the widths of gaps for

LRM and LRMd along other lines of sight but the variations are within the statistical errors.

On the other hand, the spectrum for the LRMc is quite different from the spectra of LRM or LRMd. This is expected as the LRMc is very different from the other two in its physical properties. As discussed in Appendix B, LRMc consists of very large neutral

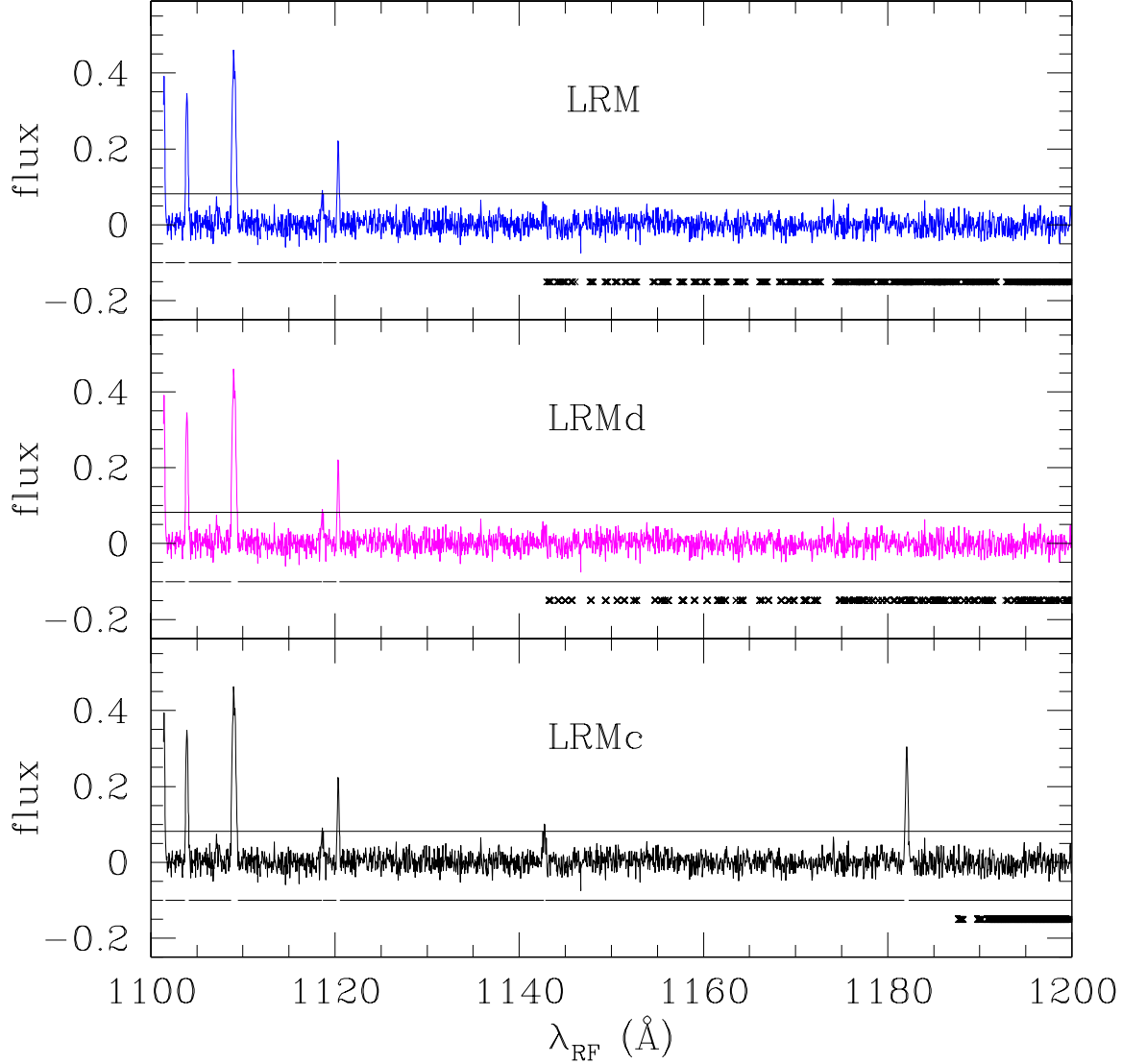


**Figure 16.** Simulated spectra for three different models of late reionization. The top panel shows a line of sight spectrum for LRM (same as in the bottom panel of Figure 8); the middle and bottom panels show spectra along the same line of sight (i.e., having the same density distribution) for LRMd and LRMc respectively. The black lines plotted immediately below the spectra show the regions identified as gaps. The positions of the neutral pixels are identified by crosses.

segments (up to 100 comoving Mpc), while the LRM and LRMd are characterized by numerous regions of smaller sizes. Since the neutral regions are highly clustered in LRMc, they leave large volumes of ionized IGM. Consequentially we find that a high fraction of lines of sight (about 70 per cent at  $z = 5.7 - 6.3$  and more than 80 per cent at  $z = 6.0 - 6.6$ ) do *not* encounter any neutral segments at all. Thus statistically LRMc is expected to be the closest to ERM and should be quite different from LRM and LRMd. Even when a line of sight encounters some neutral segments, it is more likely that the segments are clustered at a few places forming large regions of neutral IGM. This can be seen in the bottom panel of Figure 16 where we find that all the neutral pixels are clustered at the highest redshift contrary to LRM and LRMd where the neutral pixels are distributed throughout the line of sight. This has a severe

effect on the distribution of gaps and peaks. For example, the peak around  $\lambda_{\text{RF}} = 1182 \text{ \AA}$  present in the ERM (see top panel of Figure 8) is completely suppressed in LRM and LRMd because of the randomly distributed neutral regions. However, the peak is present in the LRMc because the neutral pixels are distributed differently. This implies that LRMc would have gaps of smaller widths compared to LRM and LRMd and thus would be closer to the ERM in its properties. Furthermore, it is clear from Figure 16 that *a large gap does not necessarily correspond to a large neutral region*. In fact we find that smaller regions of neutral hydrogen (of sizes  $\lesssim 1$  comoving Mpc) dispersed along the line of sight are more effective in suppressing the flux and thus creating large dark gaps in the absorption spectra compared to the larger clustered regions. Probing such small regions are quite difficult with cosmological simulations

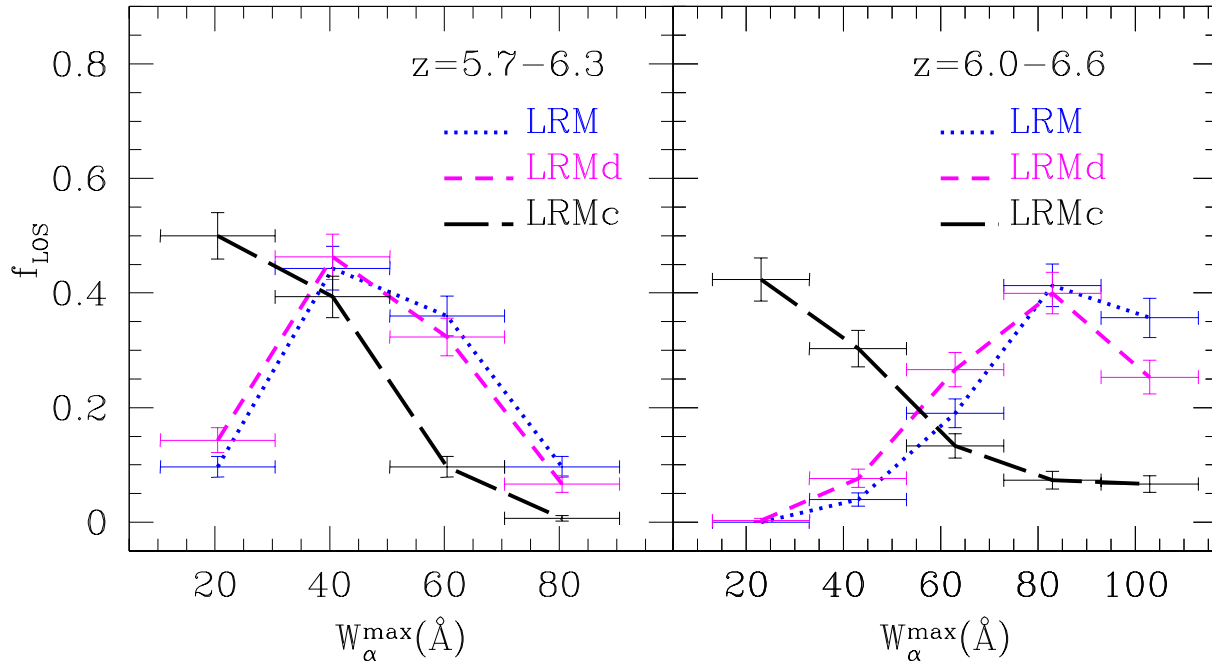


**Figure 17.** Same as in Figure 11 but considering only late reionization models. Dotted (blue), long-dashed (magenta) and long-dashed (black) lines represent LRM, LRMd and LRMc respectively.

as they are close to the resolution limits, thus semi-analytical studies can be of more help in such cases.

We can carry out more quantitative comparisons between the different reionization models. We focus on the fraction of lines of sight with a given value of largest gap width for the two redshift ranges. Our results are plotted in Figure 17. As expected, the difference between LRM and LRMd is not statistically significant. The fraction of larger dark gaps in both panels is slightly lower in the LRMd with respect to the LRM. This result can be understood noting that in the LRMd the neutral regions are preferentially located in those pixels having an higher density, where the flux is already more likely suppressed. On the contrary the distribution for LRMc is quite different and is more similar to ERM (see Figure 11). The point to note is that in spite of such extreme (and somewhat unphysical) clustering, the LRMc is still different from ERM. For example, 10 per cent of the lines of sight have a largest gap width of 60 Å (80 Å) in the range  $z = 5.7 - 6.3$  ( $z = 6.0 - 6.6$ ) for LRMc which are not present in the ERM. Thus even in the most extreme distribution of neutral regions, the ionization state of the IGM can be determined using the dark gap statistics.

Moreover, it is also interesting to note that the distribution of the largest gap is quite different for LRM and LRMc – thus it might be possible to obtain some information on the clustering of neutral regions. For example, in a quite realistic situation where we are provided with only, say, 10 QSO spectra with emission redshift above 6, we expect to find in the LRMc one LOS having a dark gap as large as 50 Å (which would rule out ERM) and, in the same sample, at least 5 LOS whose largest dark gap does not exceed 30 Å (which would rule out LRM). In this case, we could conclude at the same time that the universe is in the pre-overlap stage and that the HI regions are highly clustered.

### 3.8 Variations in the resolution and signal to noise ratio

We have carried out extensive checks on our predictions by varying different observational and instrumental artifacts. In particular, we have varied the resolution and noise in the simulated spectra to verify if any of our conclusions change.

Our results presented in the previous sections are based on a resolution of 5300, which corresponds to a FWHM of  $\sim 60 \text{ km s}^{-1}$ . We have checked our results for up to a resolution as high as 40000 (corresponding to a FWHM of  $\sim 8 \text{ km s}^{-1}$ ), which is similar to what is expected in very high quality spectra. The results, particularly the gap and peak width statistics for the Ly $\alpha$  forest do show some variations when the resolution is high. However, we find that none of our conclusions get modified in a significant way.

For the noise, we have been using a Gaussian random variate having variance  $\sigma_{\text{noise}} = 0.02$ . Decreasing the value of  $\sigma_{\text{noise}}$  (which corresponds to higher signal-to-noise ratio) has no effect on the gap and peak statistics. However, if we increase the value of  $\sigma_{\text{noise}}$  such that it becomes close to the flux threshold ( $\sim 0.08$ ) used to define the dark gaps, we find that the occurrence of gaps (and peaks) changes drastically; there are various spurious spikes which arise because of high noise. Thus, to study dark gaps in absorption spectra it is better to have a good signal-to-noise ratio; in case the signal-to-noise ratio is poor, it is necessary to use a higher flux threshold for defining the gaps.

## 4 CONCLUSIONS

In this work we have applied various statistical diagnostics to the transmitted flux of the Ly $\alpha$  (and Ly $\beta$ ) forest, with the aim of constraining cosmic reionization history. Two different reionization scenarios, based on self-consistent models of Choudhury & Ferrara (2005), have been considered: (i) an Early Reionization Model (ERM) characterized by a highly ionized IGM at  $z \lesssim 14$ , and (ii)

a Late Reionization Model (LRM) in which reionization occurs at  $z \approx 6$ . These reionization histories are the result of different assumptions about the type of ionizing sources considered. In both models, at redshifts  $z < 6$  contributions to the UV background come from PopII stars and QSOs. The main difference between ERM and LRM is constituted by the presence of PopIII stars (not included in the LRM) which reionize the IGM at high redshift in ERM. We note that for the ERM the electron scattering optical depth is  $\tau_e = 0.17$ , in agreement with the WMAP value, whereas for the LRM  $\tau_e = 0.06$ , a value more than  $2\sigma$  away from the mean. The main aim of this work is to quantitatively compare the predictions from these two models, taken as representative of a wider class of early or late reionization scenarios, with the highest quality observational data.

First, we have extensively tested our results against available data at  $z < 6$  and found that ERM and LRM are equally good at explaining the observational results. In particular, they reproduce very well the observed Gunn-Peterson optical depth evolution, the Probability Distribution Function of the transmitted flux, and the Dark Gap Width Distribution. This comparison allows us to draw a few conclusions: (i) the  $\text{Ly}\alpha$  forest observations at  $z < 6$  are unable to discriminate early vs. late reionization scenarios; (ii) the same data cannot exclude that reionization took place as early as by  $z \approx 14$ .

In order to make progress higher redshift quasar spectra are necessary, which are likely to become soon available as SDSS is expected to find  $\sim 20$  luminous quasars in the redshift range  $6 < z < 6.6$ . By extending our model predictions to higher redshifts we find that: (i) The mean and the PDF of the transmitted flux are essentially useless to constrain the ionization state at  $z \gtrsim 6$  as most of the pixels are consistent with zero transmission (independent of the ionization state), i.e. in practice these statistics probe the noise distribution; (ii) the dark gap width distribution (DGWD) is very sensitive to the reionization history. We expect at least 30 per cent of the lines of sight (accounting for statistical errors) in the range  $z = 5.7 - 6.3$  to have dark gaps of widths  $> 50 \text{ \AA}$  (in the QSO rest frame) if the IGM is in the pre-overlap stage at  $z \gtrsim 6$ , while no lines of sight should have such large gaps if the IGM is already ionized. The constraints become more stringent at higher redshifts. We find that in order to discriminate between early and late reionization scenarios 10 QSOs should be sufficient for the DGWD to give statistically robust results. (iii) The statistics of the peaks in the spectra represents an useful complement to the dark gaps and can put additional constraints on the ionization state. As for the DGWD, we find that this statistics constrains reionization models more efficiently at high redshifts. In particular, if the universe is highly ionized at  $z \sim 6$ , we expect to find peaks of width  $\sim 1 \text{ \AA}$  in 40 per cent of the lines of sight, in the redshift range  $6.0 - 6.6$ ; on the contrary, the LRM predicts no peaks larger than  $0.8 \text{ \AA}$ .

As an independent check of the models, we have extended all the above statistics to  $\text{Ly}\beta$  regions. It turns out that this diagnostics is less powerful than the analog  $\text{Ly}\alpha$  one to probe the ionization state of the IGM. Moreover, since the  $\text{Ly}\beta$  cross section is 5.27 times smaller than  $\text{Ly}\alpha$  one, the flux is always higher in the  $\text{Ly}\beta$  region than in the  $\text{Ly}\alpha$  forest. This implies that to obtain  $\text{Ly}\beta$  constraints as stringent as those from  $\text{Ly}\alpha$ , requires the analysis of QSOs spectra for  $z > 6.6$ .

We would like to comment on some additional issues concerning LRM. As discussed in the text, the hydrogen distribution in the LRM for low density IGM is characterized by two distinct phases at  $z \gtrsim 6$ , namely an ionized and a neutral phase. To model this two-

phase IGM we have studied different topologies of neutral regions. Interestingly, the main conclusions of our work remain unchanged (see for instance Figure 17) irrespective of whether we assume that the positions of the neutral regions are completely random (LRM) or we correlate the HI regions along different lines of sight with the density field (LRMd). This result is basically due to the damping wings of neutral regions, which are able to suppress the flux in regions of the spectra that are fully ionized (See Figure 9). On the other hand if the suppression of the flux does not necessarily correspond to the presence of neutral regions, it implies that QSO spectra might not be very useful to study in details the topology of the neutral hydrogen.

However it is still possible to get some idea about the clustering of the neutral regions *provided we know the evolution of the volume filling factor of ionized regions reasonably well*. We have studied an alternative distribution of the neutral regions, called LRMc, where we assume that neutral regions form the largest possible coherent structure along the line of sight (sometimes as large as 100 Mpc comoving which corresponds to almost 1/3 of the box). Because of such high clustering, large volumes of IGM are left ionized, resulting in a large fraction of lines of sight which do *not* encounter any neutral region at all. Consequently, the distribution of the largest dark gap widths is biased towards lower widths compared to LRM. This means that the statistics of the largest dark gaps could also give an idea of the clustering in the HI regions. Moreover, as is well known, the 21 cm signal from neutral hydrogen is sensitive to distribution of the HII regions (Furlanetto, Hernquist, & Zaldarriaga 2004; Furlanetto, Zaldarriaga, & Hernquist 2004). Hence 21 cm maps could be promising to study the correlation between neutral regions and to obtain a more detailed and quantitative analysis of the size of neutral regions.

Comparing the LRM and LRMc, we also find that *a large gap does not necessarily correspond to a large neutral region*. In fact smaller regions of neutral hydrogen (of sizes  $\lesssim 1$  comoving Mpc) dispersed along the line of sight are more effective in suppressing the flux (because of damping wings) and thus creating large dark gaps in the absorption spectra compared to the larger clustered regions. Probing such small regions is quite difficult with cosmological simulations as they are close to the resolution limits, thus semi-analytical studies can be more helpful in such cases. Our method, in fact, does not suffer of spurious resolution effects. At high redshift, the length of dark gaps can be  $\gtrsim 60$  Mpc and hence the analysis requires a large sample of very long lines of sight. In order to create realizations of such long lines of sight, numerical simulations typically sample different regions of the box more than once (the so-called “oversampling” effect; Paschos & Norman 2005) or combine various spectra of smaller sizes end-to-end (F02). It is difficult to obtain the distribution of very large gaps (which are much larger than the box sizes) from such procedures as multiple ray passages through the same box could produce spectacular spurious artifacts in the gap statistics. For example, we find a much better match with the observations of dark gap width distribution when compared to the simulations of Paschos & Norman (2005), who have used a box of size  $6.8 h^{-1} \text{ Mpc}$ .

However, our method suffers from some limitations which are worth noting. First, we are not able to tackle the non-linearities in any self-consistent formalism – instead we assume a density distribution for the baryons (lognormal, in this case). Since the  $\text{Ly}\alpha$  and  $\text{Ly}\beta$  forests in the QSO absorption spectra arise from mostly quasi-linear regime, the approximation should be reasonable for computing the transmitted flux. Second, it is nearly impossible to include full radiative transfer effects in our computation of the distribution

of the neutral regions and also we are not able to take into account the clustering of sources which is crucial to understand the properties of ionized bubbles. However it is most likely that the location of ionizing sources might not be significantly correlated with neutral regions, particularly when one is dealing with high values of filling factor, as in our case (see, for example, the maps in Figure 1 of Ciardi, Ferrara, & White 2003). Anyway it would be interesting to combine our approach in the distribution of neutral regions with radiative transfer simulations for a more detailed analysis of the absorption spectra, particularly in the vicinity of the QSO (which corresponds to a highly non-linear structure which is beyond the validity of the lognormal approximation).

In the future, it would be most interesting to check our predictions against a large sample of high signal-to-noise QSO data at redshift  $> 6$ . Our results show that in that case the dark gap statistics would provide a robust and independent probe of the reionization history.

## ACKNOWLEDGMENT

We acknowledge useful discussions with G. Becker, L. Cowie, S. Cristiani, X. Fan, M. Haehnelt, A. Nusser, W. Sargent, J. Schaye, A. Songaila, M. Strauss, T. Theuns, M. Viel. A special thank goes to N. Gnedin for generously providing us with the HydroPM code. We thank the referee for useful comments which have helped in improving the clarity of the paper.

## REFERENCES

Bardeen J. M., Bond J. R., Kaiser N., Szalay A. S., 1986, *ApJ*, 304, 15  
 Becker R. H. et al., 2001, *AJ*, 122, 2850  
 Bi H., 1993, *ApJ*, 405, 479  
 Bi H. G., Börner G., Chu Y., 1992, *A&A*, 266, 1  
 Bi H., Davidsen A. F., 1997, *ApJ*, 479, 523  
 Bolton J. S., Haehnelt M. G., Viel M., Springel V., 2005, *MNRAS*, 357, 1178  
 Chen X., Miralda-Escudé J., 2004, *ApJ*, 602, 1  
 Chiu W. A., Fan X., Ostriker J. P., 2000, *ApJ*, 534, 507  
 Chiu W. A., Ostriker J. P., 2000, *ApJ*, 534, 507  
 Choudhury T. R., Ferrara A., 2005, *MNRAS*, 361, 577  
 Choudhury T. R., Padmanabhan T., Srianand R., 2001, *MNRAS*, 322, 561  
 Choudhury T. R., Srianand R., Padmanabhan T., 2001, *ApJ*, 559, 29  
 Ciardi B., Ferrara A., 2005, *Space Sci. Rev.*, 116, 625  
 Ciardi B., Ferrara A., White S. D. M., 2003, *MNRAS*, 344, L7  
 Coles P., Jones B., 1991, *MNRAS*, 248, 1  
 Croft R. A. C., 1998, in Olinto A. V., Frieman J. A., Schramm D. N. ed., *Eighteenth Texas Symposium on Relativistic Astrophysics*. World Scientific, River Edge, N. J., p. 664  
 Fan X. et al., 2001, *AJ*, 122, 2833  
 Fan X., Narayanan V. K., Strauss M. A., White R. L., Becker R. H., Pentericci L., Rix H., 2002, *AJ*, 123, 1247  
 Fan X. et al., 2003, *AJ*, 125, 1649  
 Fan X. et al., 2005, *astro-ph/0512082*  
 Furlanetto S. R., Hernquist L., Zaldarriaga M., 2004, *MNRAS*, 354, 695  
 Furlanetto S. R., Zaldarriaga M., Hernquist L., 2004, *ApJ*, 613, 16  
 Furlanetto S. R., Zaldarriaga M., Hernquist L., 2005, *astro-ph/0507266*  
 Furlanetto S. R., Oh S. P., 2005, *MNRAS*, 363, 1031  
 Gnedin N. Y., 2004, *ApJ*, 610, 9  
 Gnedin N. Y., 2000, *ApJ*, 542, 535  
 Gnedin N. Y., Hui L., 1998, *MNRAS*, 296, 44  
 Haiman Z., Holder G. P., 2003, *ApJ*, 595, 1  
 Haiman Z., Cen R., 2005, *ApJ*, 623, 627  
 Hui L., Gnedin N. Y., 1997, *MNRAS*, 292, 27

Kogut A. et al., 2003, *ApJS*, 148, 161  
 Madau P., Ferrara A., Rees M. J., 2001, *ApJ*, 555, 92  
 Malhotra S., Rhoads J. E., 2004, *ApJ*, 617, L5  
 Malhotra S., Rhoads J. E., 2005, *astro-ph/0511196*  
 Mesinger A., Haiman Z., 2004, *ApJ*, 611, L69  
 Nagamine K., Cen R., Hernquist L., Ostriker J. P., Springel V., 2004, *ApJ*, 610, 45  
 Nusser A., Benson A. J., Sugiyama N., Lacey C., 2002, *ApJ*, 580, L93  
 Paschos P., Norman M. L., 2005, *ApJ*, 631, 59  
 Peebles P. J. E., 1993, *Principles of physical cosmology*. Princeton, NJ: Princeton University Press  
 Rauch M. et al., 1997, *ApJ*, 489, 7  
 Schaye J., Theuns T., Leonard A., Efstathiou G., 1999, *MNRAS*, 310, 57  
 Schaye J., Theuns T., Rauch M., Efstathiou G., Sargent W. L. W., 2000, *MNRAS*, 318, 817  
 Shull J. M., van Steenberg M. E., 1985, *ApJ*, 298, 268  
 Songaila A., 2004, *AJ*, 127, 2598  
 Songaila A., Cowie L. L., 2002, *AJ*, 123, 2183  
 Spergel D. N. et al., 2003, *ApJS*, 148, 175  
 Storrie-Lombardi L. J., McMahon R. G., Irwin M. J., Hazard C., 1994, *ApJ*, 427, L13  
 Sugiyama N., 1995, *ApJS*, 100, 281  
 Theuns T., Leonard A., Efstathiou G., Pearce F. R., Thomas P. A., 1998, *MNRAS*, 301, 478  
 Viel M., Matarrese S., Mo H. J., Haehnelt M. G., Theuns T., 2002, *MNRAS*, 329, 848  
 Wyithe J. S. B., Loeb A., 2004, *Nat*, 432, 194  
 Wyithe J. S. B., Loeb A., Carilli C., 2005, *ApJ*, 628, 575  
 Yu Q., Lu Y., 2005, *ApJ*, 620, 31

## APPENDIX A: LOGNORMAL APPROXIMATION VS. SIMULATIONS

In this Appendix we compare the various  $\text{Ly}\alpha$  flux statistics, namely, the PDF and DGWD, computed using the lognormal model with those obtained from numerical simulations. Of course, a thorough verification of the lognormal approximation would require a comparison with full hydrodynamical simulations; however, since it has been found that the HydroPM simulations are able to reproduce most of the physical properties of the  $\text{Ly}\alpha$  forest and are computationally much less expensive, we shall restrict ourselves to HydroPM simulations for the purpose of this work. We should mention here that the comparison presented here is mainly to justify the lognormal approximation for doing statistics with  $\text{Ly}\alpha$  forest at  $z \approx 6$  – this is not intended to be a rigorous justification for the lognormal approximation for the baryonic density field.

While comparing our model with HydroPM simulations, one should keep in mind that the two models are *not at all* similar in their treatment of the reionization histories. While our models treat the reionization as an extended and gradual process with different ionized regions overlapping gradually, the simulations consider an abrupt reionization. Since sorting out such issues require much detailed effort, we restrict the comparisons in the post-reionization epoch (i.e.,  $z < 6$ ) and choose the parameters (cosmological model,  $T_0$ ,  $\gamma$ ,  $\Gamma_{\text{HI}}$ ) in our code in a manner that they have the same values as HydroPM simulations at  $z < 6$ . This allows us to have a fair comparison between the lognormal model and numerical simulations with uncertainties due to different reionization histories under control. Note that, for the comparison in this Appendix, we have *not* used the reionization models (LRM or ERM) described in the paper – in fact, we have used the values from the HydroPM code.

We have run HydroPM simulations with  $128^3$  particles in a  $12.8h^{-1}$  Mpc box having a mesh size of  $100h^{-1}$  kpc. At various

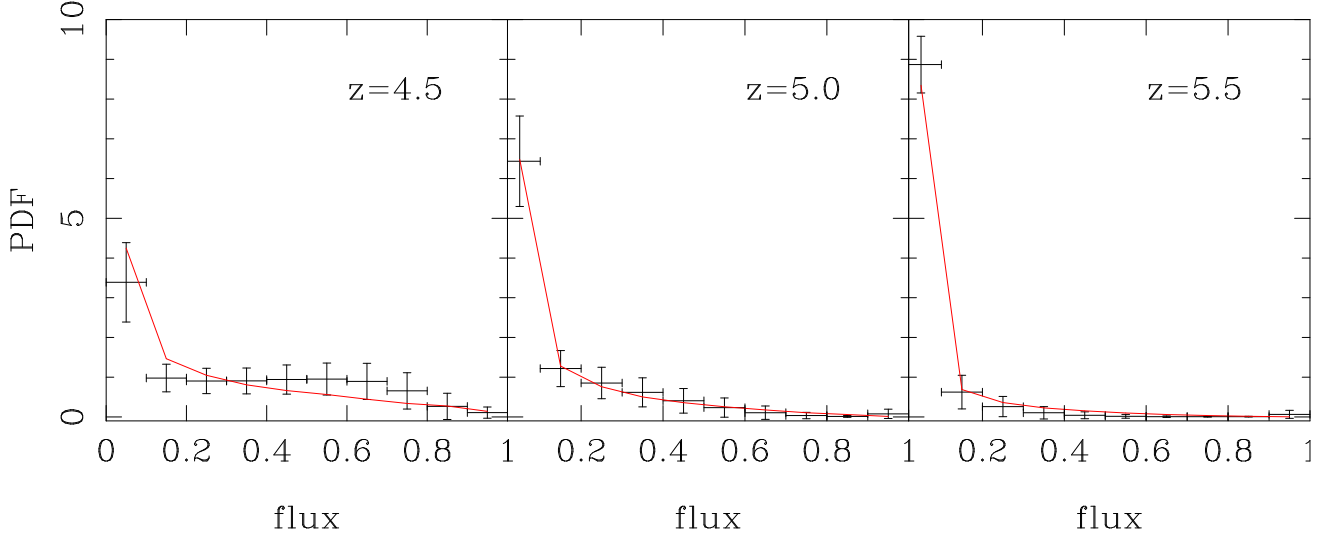


**Figure A1.** Comparison of the PDF of transmitted flux obtained from lognormal model, shown as solid lines, with that obtained from HydroPM simulations, shown as points with error bars. The vertical error bars represent dispersion along different lines of sight, while the horizontal error bars denote the bin size. We show the results for three redshifts  $z = 4.5$  (left panel),  $z = 5.0$  (middle panel) and  $z = 5.5$  (right panel).

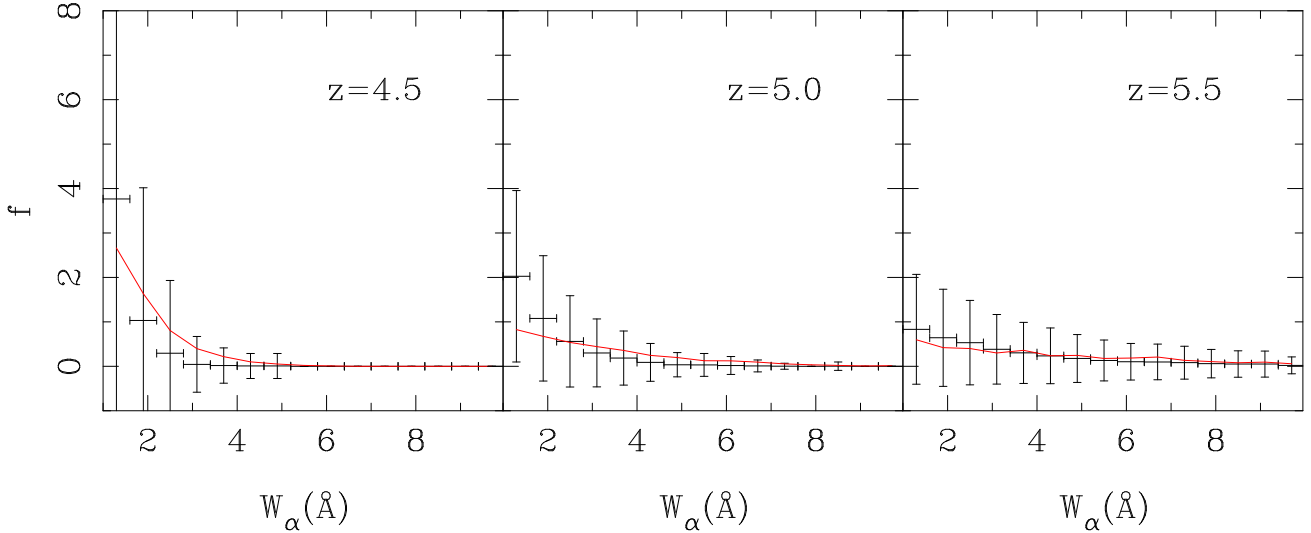


**Figure A2.** Same as in Figure A1 but for DGWD.

redshift outputs, random LOS were chosen along different directions and the corresponding density and velocity fields were calculated. It is then straightforward to obtain the transmitted flux along the LOS given the values of different parameters related to the IGM. In the case of the lognormal model, we use the same procedure outlined in Section 2. We use a box size and resolution similar to what is used in the numerical simulations so that the resolution effects are not substantial. We have *not* added any observational artifacts (smoothing, noise etc) so that the comparison is restricted to physical properties of the IGM. We compute the PDF and DGWD in a manner similar to what is described in the main text.

The results for PDF and DGWD are shown in Figures A1 and A2 respectively for three redshifts 4.5, 5.0 and 5.5. At redshifts lower than 4.5, the frequency of gaps reduces considerably and hence, in some sense, the usefulness of the gap statistics becomes irrelevant. On the other hand, at higher redshifts, the size of the gaps become of the order or larger than the box size of the HydroPM simulations, and hence one needs to use considerably larger

box sizes to carry out the comparison. Furthermore, at redshifts closer to 6, the physical properties of the IGM might be affected by details of the reionization history (particularly if the reionization is late), and hence we restrict ourselves to  $z < 5.5$ .

As can be seen from the Figure, the agreement between lognormal approximation and HydroPM simulations is excellent at  $z = 5.5$ , both for the PDF and the DGWD. The agreement is slightly less for  $z = 5.0$  and is acceptable (within  $1\sigma$ ) at  $z = 4.5$ . It is thus clear that the lognormal model can be used reliably for Ly $\alpha$  transmitted flux statistics, particularly at high redshifts.

## APPENDIX B: VOLUME FILLING FACTOR OF IONIZED REGIONS

In Sections 2.1 and 2.2 physical properties of different reionization models have been discussed. In particular it results that in the Late Reionization Model (LRM) the IGM is characterized by two dis-

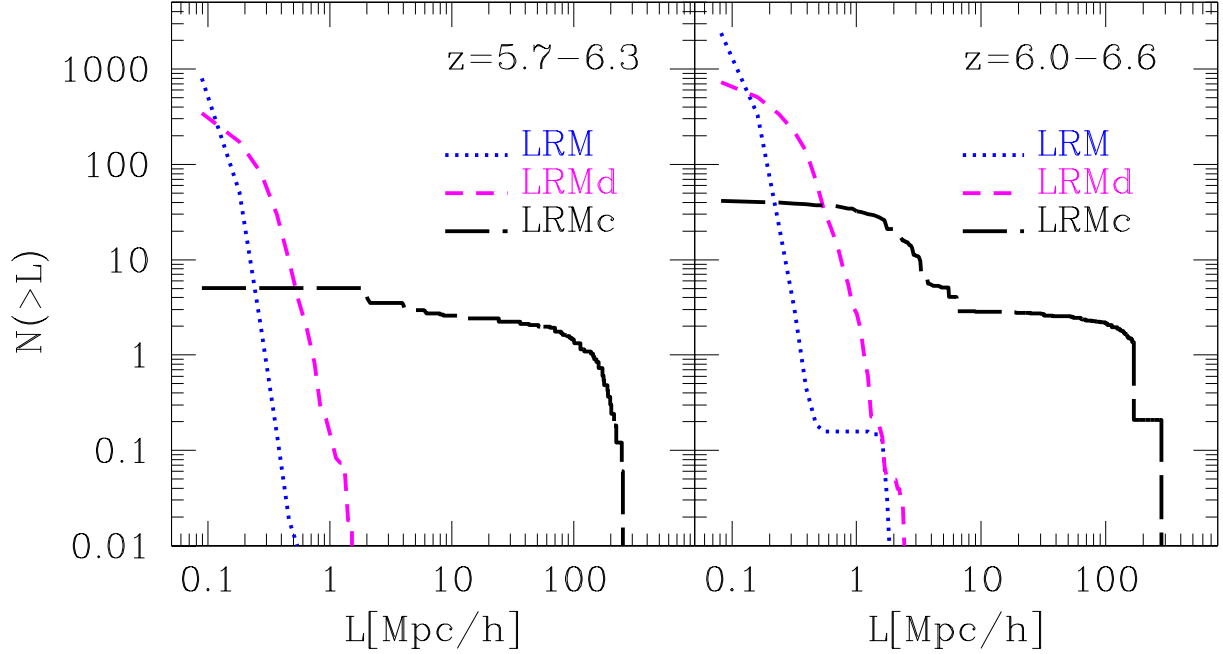


**Figure A3.** Cumulative distribution of the lengths of the neutral regions in the redshift ranges 5.7–6.3 (left panel) and 6.0–6.6 (right panel) for three different reionization models as indicated in the figure.

tinct phases at  $z \gtrsim 6$ , namely an ionized and a neutral phase. The aim of this Appendix is to explain how we distribute the fully neutral regions along different lines of sight in the LRM, taking into account the scatter and evolution in the volume filling factor  $Q_{\text{HII}}(z)$  of ionized regions. The method consists of two parts which are described in the two following subsections:

### B1 Calculation of the one dimensional filling factor $q_{\text{HII}}(z)$

This involves the geometrical translation of the three-dimensional filling factor  $Q_{\text{HII}}(z)$  to a distribution of the one dimensional filling factor  $q_{\text{HII}}(z)$  along different lines of sight. This calculation can be performed once  $Q_{\text{HII}}(z)$  and the geometry of the neutral regions are known.

We start the procedure with a three-dimensional box with two spatial directions (representing two directions on the sky) and one direction along the redshift axis (representing the direction along the line of sight). The spatial extent of the box can be arbitrary as we are only doing a geometrical exercise. We divide the box into (thin) redshift slices and within each slice distribute a number of neutral regions according to the value of  $Q_{\text{HII}}(z)$  at that redshift. Note that this procedure automatically takes into account the evolution in the volume filling factor. However, the value of  $Q_{\text{HII}}(z)$  at a redshift does not contain information of the typical sizes and shapes of the neutral regions. We thus consider the two most extreme cases, one in which the neutral regions are distributed in a completely random manner with no clustering, while in the other case we put *maximally correlated* neutral regions which are of the largest size allowed by the value of  $Q_{\text{HII}}(z)$  at that given redshift. In the first case, the box is characterized by numerous neutral regions of very small sizes, while in the second one, the box consists of bigger neutral blobs representing the maximum clustering of neutral regions. While in reality, none of these cases may represent the geometry of the neutral regions, they nevertheless repre-

sent the two extremes and thus we are sure that the actual case is somewhere between these.

Once we have distributed the neutral regions within the three-dimensional box, we shoot numerous lines of sight through it. Each line of sight intersects different neutral regions at different redshifts, and thus we can calculate the one-dimensional filling factor  $q_{\text{HII}}(z)$  along each of them. Thus given a single  $Q_{\text{HII}}(z)$ , we build up a distribution of  $q_{\text{HII}}(z)$  characterizing each line of sight. Using this distribution, we are not only able to take into account the evolution in  $Q_{\text{HII}}(z)$ , but also the intrinsic scatter (or, cosmic variance) in the distribution of neutral regions.

### B2 Correlation between neutral regions and the density field

Now that we have found out (at least) two ways of calculating  $q_{\text{HII}}(z)$  along a given line of sight, we have to accordingly distribute the neutral pixels along the same. For this, it is essential that we know whether the neutral regions have any correlation with the density field. The Ly $\alpha$  forest arises mostly from baryonic overdensities of a few ( $\lesssim 5$ ) and it is not clear whether the neutral regions have any correlation with densities within such ranges (the correlation is much more established in case of higher densities). Hence we have tried both the options; in the first case, we have distributed the neutral pixels along the line of sight without any consideration for the density field, while in the second case we distribute the neutral pixels such that high density regions are preferentially neutral at the same time preserving the evolution trend of  $q_{\text{HII}}(z)$ .

### B3 Different LRMs

Since we have two ways of calculating the one-dimensional filling factor and furthermore have the freedom in choosing whether the neutral regions are correlated with the density field, we can devise various LRMs which will cover all the extreme possibilities of distributing the neutral regions.

- **LRM:** While computing the distribution of the one-dimensional filling factor, we assume that the neutral regions are distributed randomly, and while distributing the neutral pixels along lines of sight, we assume that they have *no* correlation with the density field. This acts as the fiducial model for our paper.

- **LRMd:** This is similar to LRM except that within a given redshift slice the neutral pixels are correlated with the density field with high density regions being preferentially neutral.

- **LRMc:** In this model we want to reach the maximum level of clustering for neutral regions. To do this we assume that neutral regions are coherent structures (resembling filaments extended along the lines of sight) which preserve the evolution of the volume filling factor. Once we assume this, we find that the IGM is characterized by highly clustered large neutral regions (of lengths as large as few tens of comoving Mpc) and the correlation of these regions with the density field does *not* have any effect on the simulated spectra.

To understand the physical properties of the different LRMs, it is useful to compute the distribution of sizes of the neutral regions along all the LOS. The number of regions  $N(> L)$  along different lines of sight having a length greater than  $L$  for two redshift intervals of interest is plotted in Figure A3. We have normalized the distribution such that the total length of the line of sight is  $1h^{-1}$  Gpc, so as to compare our results to those obtained from simulations (Nusser et al. 2002).

The first obvious fact to note by comparing the two panels of the Figure is that, for a given model, the number of neutral regions with comparatively larger sizes increases as one goes to higher redshifts. Furthermore, it is also clear that the LRMc consists of very large regions ( $\sim 10\text{--}100 h^{-1}$  comoving Mpc) as it represents the model with maximum clustering of neutral regions. Among the other two models (LRM and LRMd), the LRMd has regions of relatively larger lengths; the reason is because of the correlation with density field. The LRM contains *no* clustering of the neutral regions and thus, as expected, is characterized by numerous regions of small sizes ( $\lesssim$  few comoving Mpc).

As an independent check on our procedure, Figure A3 can be compared with Fig. 1 of Nusser et al. (2002) in a qualitative manner. Nusser et al. (2002) use N-body simulations coupled to a semi-analytical galaxy formation model and various models of propagation of ionization fronts to calculate the sizes of neutral segments along lines of sight. Since our method for calculating the reionization history is quite different from theirs, it is not possible to carry out a more quantitative comparison. Even though our modelling of neutral regions predicts a larger number of small regions than simulations, we have to keep in mind that our resolution in computing the QSO spectra is much higher than simulations (in our case it is  $\sim 0.04h^{-1}$  Mpc while in the simulations of Nusser et al. 2002 it is  $\sim 0.55h^{-1}$  Mpc). As also claimed by Nusser et al. (2002), the lengths of neutral regions depend on the resolution adopted in the computation, i.e., increasing the resolution increases the number of small regions. As a check, when we compute the distribution of neutral regions using a resolution close to Nusser et al. (2002) one, we find that our results are in good agreement with simulations in the LRM/LRMd cases, thus supporting the reliability of our approximate method of distributing neutral regions, while LRMc results to be quite distant from the simulation results as it produces segments as large as  $100 h^{-1}$  comoving Mpc which are never seen in simulations; nevertheless we study it as an extreme case.

We end this Appendix pointing to the fact that the numerical simulations cannot probe lengths much smaller than  $1 h^{-1}$  comoving Mpc because of resolution effects; however with our semi-

analytical models, it is possible to probe neutral regions with sizes as small as  $0.04 h^{-1}$  comoving Mpc. Interestingly, it turns out that these small regions, distributed randomly, are as effective as larger regions in suppressing the flux of the quasar spectra. This issue has been discussed in great detail in Section 3.7.